The FBXO45-GEF-H1 axis controls germinal center formation and B-cell lymphomagenesis

Anagh A. Sahasrabuddhe[1,21,22] Xiaofei Chen[2, 22], Kaiyu Ma[3, 22], Rui Wu[1,21], Huan-Chang Liang[1, 21], Richa Kapoor[4], Rishi R. Chhipa[4], Ozlem Onder[4], Courtney McFetridge[4], John S. Van Arnam[4], Xiao Zhang[5], Jennifer J.D. Morrissette[4], Vinodh Pillai[4], Marilyn M. Li[4], Philippe Szankasi[6], Venkatesha Basrur[7], Kevin P. Conlon[7], Tobias D. Raabe[8], Nathanael G. Bailey[9], Cory M. Hogaboam[10], Robert Rottapel[11,12], Junhyong Kim[13], Cristina López[14], Matthias Schlesner[15], Reiner Siebert[14], Kostiantyn Dreval[16,17], Ryan D. Morin[16,17], Loredana Moro[1,21], Michele Pagano[18,19], Louis M. Staudt[20], Megan S. Lim[1,21] and Kojo S. J. Elenitoba-Johnson[1, 21]*

[1] Department of Pathology and Laboratory Medicine, Memorial Sloan Kettering Cancer Center, New York, NY 10065, USA

[2] Eppendorf Americas, 100 Crossing Blvd, Framingham, MA 01702, USA

[3] Department of Dermatology, University of Pennsylvania Perelman School of Medicine, Philadelphia, PA 19104, USA

[4] Department of Pathology and Laboratory Medicine, University of Pennsylvania Perelman School of Medicine, Philadelphia, PA 19104, USA

[5] Division of Bone and Mineral Diseases, Washington University School of Medicine, St. Louis, MO, USA.

[6]ARUP Laboratories, Salt Lake City, UT 84108, USA

[7] Department of Pathology, University of Michigan Medical School, Ann Arbor, MI 48109, USA

[8] Division of Translational Medicine, Perelman School of Medicine, University of Pennsylvania, Philadelphia, PA 19104, USA

[9] Department of Pathology, University of Pittsburgh, Pittsburgh, PA 15213, USA

[10] Department of Pulmonary and Critical Care Medicine, Cedars-Sinai Medical Center, Los Angeles, CA 90048, USA

[11] Princess Margaret Cancer Centre, Toronto Medical Discovery Tower, Toronto, ON M5G 1L7, Canada

[12] Department of Medicine, University of Toronto, Toronto, ON M5G 1L7, Canada

[13] Department of Biology, University of Pennsylvania, Philadelphia PA 19104, USA

[14] Institute of Human Genetics, Ulm University and Ulm Medical Center, Ulm 89081, Germany

[15] Biomedical Informatics, Data Mining and Data Analytics, Faculty of Applied Computer Science and Medical Faculty, University of Augsburg, Augsburg, DE-BY 86159, Germany
[16] Canada's Michael Smith Genome Sciences Center, BC Cancer Research Centre, Vancouver, BC V5Z 1L3, Canada.
[17] Department of Molecular Biology and Biochemistry, Simon Fraser University, Burnaby, BC V5A 1S6, Canada
[18] Department of Biochemistry and Molecular Pharmacology, Laura and Isaac Perlmutter NYU Cancer Center, NYU Grossman School of Medicine, New York, NY 10016, USA.
[19] Howard Hughes Medical Institute, New York, NY 10065, USA
[20] Lymphoid Malignancies Branch, Center for Cancer Research, National Cancer Institute, National Institutes of Health, Bethesda, MD 20892, USA
[21] Human Oncology Pathogenesis Program, Memorial Sloan Kettering Cancer Center, New York, NY 10065, USA
[22]These authors contributed equally.

Corresponding authors*:
Kojo S. J. Elenitoba-Johnson, MD
Memorial Sloan Kettering Cancer Center
Department of Pathology and Laboratory Medicine
1275 York Avenue, New York, NY 10065, USA
Telephone: (212) 639-2410
Email address: elenitk@mskcc.org

Megan S. Lim, MD, PhD
Memorial Sloan Kettering Cancer Center
Department of Pathology and Laboratory Medicine
417 East 68th Street, New York, NY 10065, USA
Telephone: (646) 888-3790
Email address: limm4@mskcc.org

Running title: FBXO45-mediated GEF-H1 degradation inhibits B-cell lymphoma.

Authors' Disclosures

MP is or has been an advisor for and has financial interests in SEED Therapeutics, Triana Biomedicines, CullGen, Kymera Therapeutics, Sibylla Biotech, and Umbra Therapeutics, and the findings presented in this manuscript were not discussed with any person in these companies. The other authors declare no competing interests. The authors acknowledge the ICGC MALY-DE project (https://dcc.icgc.org) for providing access to their data. Aligned reads for those genomes were obtained through a DACO-approved project (R.D.M.) using a virtual instance on the Cancer Genome Collaboratory. The results published here are in whole, or part, based on data generated by the Cancer Genome Characterization Initiative (phs000235), Non-Hodgkin Lymphoma project, developed by the National Cancer Institute. The data used for this analysis are available at https://www.ncbi.nlm.nih.gov/projects/gap/cgi-bin/study.cgi?study_id=phs000235.v20.p6. Information about Cancer Genome Characterization Initiative projects can be found at https://ocg.cancer.gov/programs/cgci.

ABSTRACT

The role of ubiquitin-mediated degradation mechanisms in the pathogenesis of diffuse large B cell (DLBCL) and follicular lymphoma (FL) is not completely understood. We show that conditional deletion of the E3 ubiquitin ligase *Fbxo45* in germinal center B-cells results in B-cell lymphomagenesis in homozygous (100%) and heterozygous (48%) mice. Mechanistically, FBXO45 targets the *RHO* guanine exchange factor ARHGEF2/GEF-H1 for ubiquitin-mediated degradation. Double genetic ablation of *Fbxo45* and *Arhgef2* ameliorated lymphoma formation. Transgenic knock-in mice harboring a GEF-H1 mutant unable to bind FBXO45 develop B-cell lymphomas with ~50% penetrance. Genome sequencing in human lymphomas identified mutually-exclusive *FBXO45* copy number losses and *ARHGEF2* gains, with combined frequencies ranging from 26.32% in FL to 45.12% in DLBCL. Notably, *FBXO45* silencing enhances sensitivity to MEK1/2 inhibition. These results identify *FBXO45* and *ARHGEF2* as a novel tumor-suppressor and oncogene pair involved in the pathogenesis of B-cell lymphomas with significant implications for targeted therapies.

STATEMENT OF SIGNIFICANCE

We describe the identification of a previously unrecognized ubiquitin ligase-substrate (FBXO45-GEF-H1) regulatory axis that plays an important role in germinal center formation and pathogenesis of common B cell lymphomas. These studies reveal novel insights linking dysregulated ubiquitin-mediated control to exploitable vulnerabilities and novel therapeutic strategies for these cancers**.**

INTRODUCTION

The germinal center (GC) is the principal microanatomic compartment for generation of specialized B cells that produce high affinity antibodies and is the origin of the vast majority of non-Hodgkin lymphomas (NHL) which remain a leading cause of cancer death in the United States (1,2). B-cell lymphomas account for the vast majority of these neoplasms, and include diffuse large B-cell lymphoma (DLBCL), which is the most frequent (25-30%) and follicular lymphoma (FL), the second most frequent (20-30%) subtypes of NHL, respectively (2). DLBCL is aggressive while FL is indolent but typically incurable (3) . DLBCL may arise *de novo*, or occur from evolution or transformation from a pre-existing low-grade lymphoma, particularly FL at an estimated annual risk of transformation of 3% (4,5)**.** Current therapies for DLBCL or transformed lymphoma involve immunochemotherapy, and refractoriness and relapse occur with an incidence of up to 40% resulting in eventual death. While the molecular mechanisms underlying the pathogenesis and evolution of these tumors are not completely understood, a recognized theme is the subversion of signaling pathways that regulate the normal B-cell GC reaction and differentiation, resulting in neoplastic transformation of lymphoid cells reflecting the dysregulated biological programs and networks (6,7). Improved understanding of the mechanisms underlying GCB-cell lymphoma pathogenesis would facilitate development of precision therapies.

E3 ubiquitin ligases are key regulators of critical cellular processes such as cell cycle progression, differentiation and apoptosis (8), and are increasingly implicated in cancer pathogenesis (9). F-box proteins are the substrate-specific adaptor subunits of the S-phase kinase associated protein 1 (SKP1), Cullin 1 (CUL1), F-box protein (SCF) E3 ubiquitin ligase complexes that promote proteasomal degradation of hundreds of critical cellular regulators (10-17). Of the 69 known human F-box proteins, FBXO45 is the only one known to contain a SPRY domain and is one of only six F-box proteins that are conserved in metazoans (13). Previous studies have shown that in contrast to other F-box proteins that assemble SCF ubiquitin ligase complexes, FBXO45 forms an atypical ubiquitin ligase complex that contains SKP1 and protein-associated with MYC (PAM), a Ring-finger protein also known as MYC-binding protein 2 (MYCBP2) (18,19). Constitutional knockout of *Fbxo45* results in perinatal mortality due to respiratory distress from abnormal neural development and impaired synapse formation at

neuromuscular junctions with defective diaphragmatic innervation (18). No known functions have been described for FBXO45 in the hematopoietic or immune system.

The small guanine nucleotide-binding proteins of the RAS homology family (RHO-GTPases) are important bimolecular switches that control signaling pathways involved in diverse cellular processes (20). Guanine nucleotide exchange factors (GEFs) catalyze activation of GTPases by stimulating the exchange of GDP for GTP and inactivation of GTPase-activating proteins that promote GTP hydrolysis (21). The guanine nucleotide exchange factor H1 (GEF-H1) encoded by the RHO guanine nucleotide exchange factor 2 (*ARHGEF2*) gene is a RHO GEF (21-23). *ARHGEF2* is evolutionarily conserved throughout the Euteleostomi clade that includes ~90% of all living vertebrates with homologues found in mammals, birds, fish and reptiles (24). It is most closely related to *Lfc* (23,25) and is a member of the DLBCL (Dbl) family of GEFs (26-28). *Dbl* was first identified as a transforming agent by transfection of mouse fibroblasts with DNA derived from a human DLBCL (29-31). GEF-H1 exhibits oncogenic activity in various tumor contexts (32,33) and is required for the survival of human breast, colon, lung, ovarian and pancreatic cell lines (32,34) . GEF-H1 has also been reported to contribute to hepatocellular carcinoma cell invasion (35), and breast cancer metastasis (36). However, the molecular mechanisms that underlie the ubiquitin-mediated regulation of GEF-H1 as well as its role in formation of the GCB-cell compartment and pathogenesis of human B-cell lymphoma are unexplored.

Herein, we demonstrate that GEF-H1 is a labile protein that is targeted for ubiquitin-mediated proteasomal degradation by FBXO45. We describe a novel role in GC formation and a haploinsufficient tumor suppressor role for FBXO45. We further demonstrate an oncogenic role for GEF-H1 in the most common subtypes of human B-cell lymphoma. We identified recurrent genomic alterations targeting *FBXO45* (copy number loss) and *ARHGEF2* (copy number gains) in the two most common subtypes of B-cell lymphoma, DLBCL and FL. Transgenic mice with conditional knockout of *Fbxo45* in GCB-cells exhibit expansion of the GCB-cell compartment and subsequent development of GCB-cell lymphoma with 100% penetrance. FBXO45 promotes GEF-H1 ubiquitylation and proteasomal degradation, thereby modulating GEF-H1-mediated activation of RhoA and MAPK downstream signaling, as well as GEF-H1 oncogenicity in B-cells. We further show that FBXO45 deficiency confers enhanced sensitivity to ERK1/2 inhibitor treatment. Overall, our studies uncover a novel FBXO45-GEF-H1 axis that regulates GC

formation and that is frequently disrupted in the most common subtypes of B-cell lymphomas. Finally, we demonstrate that this novel pathway represents an opportunity for novel therapeutic targeting strategies in these malignancies.

RESULTS

Differential quantitative proteomics and RNAi screen identifies *FBXO45* as a candidate tumor suppressor in DLBCL and its knockdown promotes B-cell proliferation

To identify novel proteins that play a role in FL evolution to DLBCL, we performed unbiased quantitative differential proteomic analysis comparing global protein expression of FL (n = 5) and their matched pair of transformed DLBCL samples (n = 5). Using a threshold of >2.0-fold differential expression (FDR<0.05), 8 proteins (TEX14, ANKH, RASIP1, C-REL, FBXO34, HHLA2, FBXO45, and CDKN2A) were differentially expressed, with FBXO45 being the protein quantitatively (3.0-fold; case 1 and 2.8-fold; case 2) and frequently downregulated in (2/5; 40%) in transformed DLBCL (Supplementary Fig. S1A, and S1B).

Next, we performed RNAi-mediated silencing of the genes that encode differentially expressed proteins and assessed their impact on cell viability in two GCB-derived lymphoma cell lines (BJAB, SUDHL6). While depletion of the known B-cell lymphoma oncogene, *C-REL* resulted in significant reduction of cell growth (~88%) as compared to control (BJAB; P<0.0001, SUDHL6; P<0.0003), RNAi-mediated silencing of the established tumor suppressor cyclin dependent kinase inhibitor 2A (*CDKN2A*) resulted in significant increase in cell proliferation (BJAB; ~47%, P<0.0013, SUDHL6; ~95%; P<0.0001). Importantly, *FBXO45* silencing resulted in significant increase in cell proliferation compared to control (BJAB; ~26%; P<0.003. SUDHL6; ~85%; P<0.0002) supporting its functional role as a candidate tumor suppressor in DLBCL (Supplementary Fig. S1C). Further, re-expression of inducible *FBXO45* reverted cell proliferation to levels observed in control (Supplementary Fig. S1D).

In vivo conditional targeting of *Fbxo45* in GCB-cells of transgenic mice results in abnormal GCB-cell expansion

To determine the physiologic expression of FBXO45 in the lymphoid compartment, we generated probes for *FBXO45* and performed RNA *in situ* hybridization for *FBXO45* combined

with immunohistochemistry. We observed *FBXO45* RNA (red) signals co-expressed in CD19 reactive B-cells (white) and CD4-positive T-cells (green) in lymphoid follicles of human reactive tonsils (Supplementary Fig. S1E). Additionally, qRT-PCR analysis of GCB+ B-cells, Naïve B-cells and Memory B-cells isolated by Fluorescence-activated cell sorting (FACS) analysis from reactive tonsils shows expression of *FBXO45* transcript in all three B-cell subsets. (Supplementary Fig. S1F). To examine the physiologic role of *Fbxo45* in the GC, *Fbxo45* was conditionally deleted in GCB-cells by crossing mice bearing a floxed *Fbxo45* exon2 allele (*Fbxo45*$^{fl/fl}$) with mice expressing the Cre recombinase specifically in GCB-cells (*Cγ1Cre*$^{tg/+}$) to generate mice with the following genotypes; *Fbxo45*-wild type (WT) (*Cγ1Cre*$^{tg/+}$-*Fbxo45*$^{+/+}$). *Fbxo45*-heterozygous knockout (HET) (*Cγ1Cre*$^{tg/+}$-*Fbxo45*$^{+/fl}$) and *Fbxo45*-homozygous knockout (HOM) (*Cγ1Cre*$^{tg/+}$-*Fbxo45*$^{fl/fl}$) (Fig. 1A-1D and Supplementary Fig. S2A-S2C). GCB-cells enriched from the spleen of *Cγ1Cre*$^{tg/+}$-*Fbxo45*$^{+/+}$, *Cγ1Cre*$^{tg/+}$-*Fbxo45*$^{+/fl}$ and *Cγ1Cre*$^{tg/+}$-*Fbxo45*$^{fl/fl}$ transgenic mice were analyzed by flow cytometry at 10-days post-immunization with sheep red blood cells (SRBC), a T-cell-dependent antigen that evokes a robust GC response and is required to induce the expression of Cre. SRBC-immunized *Cγ1Cre*$^{tg/+}$-*Fbxo45*$^{fl/fl}$ mice displayed 1.2 to-1.5-fold increase in both the percentage and absolute number of splenic GCB-cells by flow cytometric assessment of PNA and GL7 expression (Fig. 1A-1D and Supplementary Fig. S3A), two GCB-cell markers. This was accompanied by an increase in the ratio of total GC numbers/spleen (1.5-fold, p=0.08) (Fig. 1E), overall GC surface area/spleen (1.72-fold, p=0.027) (Fig. 1F) (n=24 for WT, n=41 for HET and n=46 for HOM knockout) and a significant increase in mean GC-size measured by PNA expression (1.7-fold, p=0.005) (n=17 for WT, n=23 for HET and n=35 for HOM knockout (Fig. 1G and 1H) in 6 month-old mice. In an independent cohort (n= 5) of WT (*Cγ1Cre*$^{tg/+}$-*Fbxo45*$^{+/+}$) and HOM (*Cγ1Cre*$^{tg/+}$-*Fbxo45*$^{fl/fl}$) mice, flow cytometric analysis corroborated observation of expansion of the germinal center compartment in Fbxo45-deficient mice (Supplementary Fig. S3B, P=0.039) in keeping with the results from previous experiments (Fig 1A and 1B). We also investigated the effect of *Fbxo45* loss on the distribution of GCB cells in the dark-zone (DZ) and light zone (LZ) by flow cytometry and observed increased proportion of DZ (median 57.9%) and correspondingly reduced proportion of LZ (median 21.2%) cells in HOM mice compared to WT (DZ, 50.38%; LZ 27.45%) resulting in increased DZ/LZ ratio in HOM mice (2.68%) compared to WT (1.9%) (P= 0.024) (Supplementary Fig. S3C-S3E). Further, cell cycle analysis of the GCB-cells from this cohort shows significantly increased proportion of cells in S-phase in HOM mice (33.46%) compared

to WT (28.1%) (p=0.031) (Fig. S3F and S3G). Taken together, these findings indicate that loss of *Fbxo45* in B-cells results in abnormal GC hyperplasia and deregulated cell cycle progression with resulting increase of GCB cells in S-phase.

In vivo conditional deletion and haploinsufficiency of *Fbxo45* in GCB-cells results in B-cell lymphomagenesis

To investigate the role of *Fbxo45* in lymphomagenesis *in vivo*, we established a cohort of mice consisting of the following genotypes; *Cγ1Cre*$^{tg/+}$-*Fbxo45*$^{+/+}$ (n = 20), *Cγ1Cre*$^{tg/+}$-*Fbxo45*$^{+/fl}$ (n = 27), and *Cγ1Cre*$^{tg/+}$-*Fbxo45*$^{fl/fl}$ (n = 20) (Fig. 2). All mice were immunized with SRBC beginning at the age of 8 weeks at monthly intervals and observed over time. Animals were euthanized and necropsied between 8 and 24 months based on moribund state of the mice. Increasing mortality was observed beginning at 12 months, such that among the *Cγ1Cre*$^{tg/+}$-*Fbxo45*$^{fl/fl}$ mice, 70% were alive at 14 months, 30% at 18 months, 10% at 21 months and 0% at 22 months. In the cohort of *Cγ1Cre*$^{tg/+}$-*Fbxo45*$^{+/fl}$ mice, 96% were alive at 14 months, 85% at 18 months, 63% at 21 months and 52% at 24 months. By comparison, 20/20 (100%) of *Cγ1Cre*$^{tg/+}$-*Fbxo45*$^{+/+}$ littermates were alive at 24 months. The median survival of *Cγ1Cre*$^{tg/+}$-*Fbxo45*$^{+/fl}$ mice was 21 months while the median survival of *Cγ1Cre*$^{tg/+}$-*Fbxo45*$^{fl/fl}$ mice was 17 months (Fig. 2A). All *Cγ1Cre*$^{tg/+}$-*Fbxo45*$^{+/+}$ littermates were alive until the end of the study (Fig. 2A).

Necropsy revealed large tumor masses and/or lymphadenopathy at various anatomic locations, namely, the ileocecal junction, mesenteric, retroperitoneal and cervical lymph nodes and thymus of *Cγ1Cre*$^{tg/+}$-*Fbxo45*$^{fl/fl}$ mice (Fig. 2B, left panel shows macroscopic images from *Cγ1Cre*$^{tg/+}$-*Fbxo45*$^{fl/fl}$ mice). A retroorbital mass was observed in one *Cγ1Cre*$^{tg/+}$-*Fbxo45*$^{fl/fl}$ mouse. Mesenteric lymph node enlargement and lymphadenopathy (Fig. 2B, right panel) was exclusively observed in *Cγ1Cre*$^{tg/+}$-*Fbxo45*$^{fl/fl}$ mice 12/20 (60%); (mesenteric LN weights 1.217g ± 0.262) while *Cγ1Cre*$^{tg/+}$-*Fbxo45*$^{+/fl}$ and *Cγ1Cre*$^{tg/+}$-*Fbxo45*$^{+/+}$ mice did not show any ($p<0.01$). Similarly, massive ileocecal masses (1.2X1.5X2.0cm^3-0.5X0.5X0.5cm^3) were exclusively observed in *Cγ1Cre*$^{tg/+}$-*Fbxo45*$^{fl/fl}$ mice (15/20; 75%) in comparison to barely visible Peyer's patches in *Cγ1Cre*$^{tg/+}$-*Fbxo45*$^{+/fl}$ (0.05X0.05X0.1cm^3) and *Cγ1Cre*$^{tg/+}$-*Fbxo45*$^{+/+}$ (0.03X0.05X0.05cm^3) animals (Fig. 2C). Specifically, 19/20 (95%) of the *Cγ1Cre*$^{tg/+}$-*Fbxo45*$^{fl/fl}$ animals exhibited significant splenomegaly (0.994g ± 0.257) as compared to 0/20 (0%) *Cγ1Cre*$^{tg/+}$-*Fbxo45*$^{+/+}$ mice (0.085g ± 0.009) (*Fbxo45*$^{fl/fl}$ vs *Fbxo45*$^{+/+}$; $P<0.0001$ (Fig. 2D).

Histological examination confirmed involvement of lymph nodes and spleen by lymphoma in all (20/20; 100%) *Cγ1Cre*$^{tg/+}$-*Fbxo45*$^{fl/fl}$ mice and in none of the *Cγ1Cre*$^{tg/+}$-*Fbxo45*$^{+/+}$ littermates (0/20; 0%) by 24 months (Fig. 2E). There was effacement of lymph node architecture and destruction of underlying local tissue by a diffuse proliferation of large lymphoid cells with centroblastic nuclei and abundant cytoplasm consistent with DLBCL (Fig. 2E). FL represented by nodular proliferations of neoplastic lymphoid cells effacing nodal or tissue architecture was also observed (Fig. 2E). Immunohistochemical analysis of the lymphomas demonstrated reactivity for B220 and PNA consistent with a GCB-cell origin (Fig. 2E). DLBCL was observed in 15/20 (75%) of *Cγ1Cre*$^{tg/+}$-*Fbxo45*$^{fl/fl}$ mice, with coexistence of DLBCL and FL in 5/20 mice (25%). FL was observed exclusively in 5/20 cases (25%) of *Cγ1Cre*$^{tg/+}$-*Fbxo45*$^{fl/fl}$ mice (Fig. 2F).

Next generation sequencing of the immunoglobulin heavy chain gene using DNA extracted from tumor obtained from *Cγ1Cre*$^{tg/+}$-*Fbxo45*$^{fl/fl}$ mice revealed prominent monoclonal populations in oligoclonal background (Fig. 2G). To confirm the tumorigenic capacity of B-cells with genetic loss of *Fbxo45*, splenic lymphomas from *Fbxo45*-deficient *Cγ1Cre*$^{tg/+}$-*Fbxo45*$^{fl/fl}$ mice (donor mice), were serially transplanted in secondary and tertiary immunodeficient NOD.Cg-*Prkdc*^{scid} *Il2rg*^{tm1Wjl}/SzJ (NSG) recipient mice (Supplementary Fig. S4). Necropsy of the secondary transplanted mice performed at day 19-20 revealed splenic involvement by lymphoma in all transplanted mice (4/4; 100%). The serial transplantation of tumor cells derived from secondary transplanted mice resulted in lymphoma development in all (6/6; 100%) tertiary recipient animals within a shorter time interval (day 14-15). Lymphomas were macroscopically manifested as massive splenomegaly (average splenic mass 1.072 g ± 0.252) with numerous visible tumor nodules (Supplementary Fig. S4A-S4C). Splenomegaly was not observed in control (non-transplanted, NT) mice that were injected with PBS (average splenic mass; 0.02 g ± 0.014) (Supplementary Fig. S4B-S4C). Histologically, spleens were infiltrated by nodular and diffuse populations of atypical lymphoid cells comprised of occasional small cleaved and predominantly large centroblastic cells representing diffuse large B-cell lymphoma (Supplementary Fig. S4D). The neoplastic cells demonstrated immunohistochemical (IHC) reactivity for CD19 and PNA and were negative for CD3 consistent with B-cell lineage and GC phenotype. Kaplan-Meier curves demonstrated median survival of 20 days in secondary recipient and 14.5 days in tertiary recipient mice, while all control mice remained alive until the end of the study (Supplementary Fig. S4E). These results indicate that primary *Fbxo45*-

deficient B-cell lymphomas from transgenic mice are serially transplantable across secondary and tertiary recipients.

In summary, *in vivo* conditional homozygous deletion of *Fbxo45* (*Cγ1cre*$^{tg/+}$-*Fbxo45*$^{fl/fl}$) in GCB-cells leads to full penetrance (100%) development of GCB-cell lymphomas (DLBCL; 75%, FL; 25%). We observed a dose-dependent effect of *Fbxo45* loss on lymphomagenesis, with ~48% and 0% penetrance in *Cγ1cre*$^{tg/+}$-*Fbxo45*$^{+/fl}$ and *Cγ1cre*$^{tg/+}$-*Fbxo45*$^{+/+}$ mice, respectively. Taken together, these findings are consistent with a haploinsufficient tumor suppressor function for *FBXO45*, and its loss in GCB-cells results in B-cell lymphomagenesis.

FBXO45 regulates GEF-H1 protein stability, RhoA activation and colony formation

Given our observation that *Fbxo45* loss results in highly penetrant B-cell lymphomagenesis, we sought to identify its candidate substrate. To identify candidate substrates of FBXO45, we utilized an integrated mass spectrometry (MS)-based approach combining immunoprecipitation (IP)-MS for FBXO45 and quantitative whole proteome analysis of pooled sorted GCB-cells from *Fbxo45* homozygous knockout (*Cγ1Cre*$^{tg/+}$-*Fbxo45*$^{fl/fl}$) mice compared with identically isolated cells from wild-type littermates (*Cγ1Cre*$^{tg/+}$-*Fbxo45*$^{+/+}$). In this regard, we isolated FBXO45 immunocomplexes from two different human B-lineage cell lines (BJAB and FL518) expressing FLAG-tagged FBXO45 followed by liquid chromatography (LC)-MS (Fig. 3A). In addition to the bait protein (FBXO45), peptides corresponding to PAM (MYCBP2) and SKP1 were identified in the IP-MS (Supplementary Table S1), consistent with previous observations (9,37). Importantly, IP-MS of both cell lines collectively yielded 29 unique peptides matching GEF-H1 (Supplementary Table S2). These peptides were not found in the negative control (FLAG-tag only) immunopurification. Quantitative whole proteome analysis of splenic GCB-cells from *Cγ1Cre*$^{tg/+}$-*Fbxo45*$^{fl/fl}$ and *Cγ1Cre*$^{tg/+}$-*Fbxo45*$^{+/+}$ mice revealed differential accumulation of proteins in the GCB-cells isolated from *Cγ1Cre*$^{tg/+}$-*Fbxo45*$^{fl/fl}$ mice (Supplementary Table S3). Integration of IP-MS with proteins that accumulated following *Fbxo45* knockout revealed 4 candidate substrates (RPS2, RPL13, RPL17 and GEF-H1) of FBXO45 (Fig. 3A) of which GEF-H1 protein was nominated as a candidate novel interactor and substrate of FBXO45.

Immunoprecipitation (IP) experiments confirmed the interaction between FLAG-FBXO45 and endogenous GEF-H1 in BJAB cells (Fig. 3B). We then sought to investigate the FBXO45-GEF-H1 interaction at endogenous levels of both proteins. To simulate endogenous FBXO45,

we utilized the CRISPR-Cas9 approach and engineered a FLAG-tag knockin at the C-terminal region of FBXO45 in K562 cells. FLAG IP of the lysate from these cells showed endogenous interaction of FLAG FBXO45 with GEF-H1 (Supplementary Fig. S5A). To investigate the specificity of the interaction, we screened eight human F-box proteins in HEK293 cells and found that only FBXO45 co-immunoprecipitated endogenous GEF-H1 (Fig. 3C). Further, FBXO45 co-immunoprecipitated its core complex components SKP1, MYCBP2 but not Cullin 1 (Fig. 3C). These experiments established exclusive interaction of FBXO45 with endogenous GEF-H1 in BJAB and HEK293 cells.

To investigate whether FBXO45 regulates GEF-H1 stability, we assessed whether *in vivo* inactivation of *Fbxo45* stabilizes GEF-H1 protein turnover. Specifically, cycloheximide pulse-chase of purified pooled splenic GCB-cells from $C\gamma1Cre^{tg/+}$-$Fbxo45^{fl/fl}$ and $C\gamma1Cre^{tg/+}$-$Fbxo45^{+/+}$ mice demonstrated stabilization of GEF-H1 protein in *Fbxo45*-KO GCB-cells ($C\gamma1Cre^{tg/+}$-$Fbxo45^{fl/fl}$) as compared to WT ($C\gamma1Cre^{tg/+}$-$Fbxo45^{+/+}$) (Fig. 3D). We knocked out *FBXO45* in K562 cells (FBXO45 KO) previously engineered to endogenously express C-terminal FLAG FBXO45 using CRISPR-Cas9 approach (Supplementary Fig. S5B) and performed cycloheximide pulse-chase experiments. We observed that turnover of endogenous GEF-H1 protein is prolonged in cells with *FBXO45* KO compared to wild-type (Supplementary Fig. S5C). To further investigate consequences of FBXO45 deficiency on GEF-H1 protein turnover, we performed cycloheximide pulse-chase experiments and examined the turnover of endogenous GEF-H1 protein in *FBXO45* knockdown cells generated using stable silencing by shRNA. We used 2 lentiviral shRNA constructs targeting *FBXO45* to generate stable *FBXO45* knockdown in BJAB cells along with a non-specific (*NS*) shRNA control. We observed that *FBXO45* shRNAs markedly reduced *FBXO45* transcript levels (Fig. 3E) and stabilized GEF-H1 protein levels (Fig. 3F). *FBXO45* silencing using *shRNA #2* prolonged the half-life of GEF-H1 in FL518 cells (Supplementary Fig. S5D). We also performed AHA-pulse labeling of nascent protein in cells with knockdown of *FBXO45* or NS control and observed that FBXO45 deficiency prolonged GEF-H1 protein turnover in BJAB cells (Supplementary Fig. S5E), while global protein synthesis remained unaltered (Supplementary Fig. S5F) (38,39). To investigate whether prolonged GEF-H1 protein turnover is due to increased RNA stability, we treated BJAB cells expressing *FBXO45* WT or *FBXO45* KO (*FBXO45* gene was knocked-out in BJAB cells by CRISPR-Cas9 and knockout was validated by Sanger sequencing, Supplementary Fig. S5G) with Actinomycin D at different time intervals. WT *FBXO45* expressing BJAB cells were used as

control. Immunoblotting of whole cell lysates showed that FBXO45 depletion increased stability of GEF-H1 protein while qRT-PCR showed steady decline in RNA levels indicating that prolonged GEF-H1 protein turnover is due to a post-transcriptional mechanism (Supplementary Fig S5H). We also observed that *shRNA*-mediated silencing of *FBXO45* promoted colony formation in BJAB cells (Fig. 3G). Having demonstrated GEF-H1 regulation by ubiquitin-mediated proteolysis, we sought to identify the condition that promotes rapid GEF-H1 protein turnover. To this end, we synchronized BJAB cells stably expressing *NS* or *FBXO45* shRNA using thymidine-nocodazole block and released cells in mitotic period. These experiments revealed that FBXO45 depletion resulted in stabilization of GEF-H1 during mitosis (Supplementary Fig. S5I).

Using a rhotekin-based GTP-RhoA binding assay which specifically detects active RhoA (34), we further observed that *FBXO45*-deficient cells exhibited prolonged RhoA activation in BJAB and FL518 cells (Fig. 3H and Fig.S5D). Finally, inducible expression of FLAG-tagged FBXO45 (iFBXO45, i = inducible) promoted rapid turnover of GEF-H1 and diminished active RhoA levels (Fig. 3I).

FBXO45-GEF-H1 axis regulates B-cell proliferation, colony formation and tumorigenesis

To assess the contribution of GEF-H1 in oncogenic transformation promoted by FBXO45 loss, cell proliferation and colony formation were assessed in BJAB and FL518 cells after co-silencing of *FBXO45* and *ARHGEF2*. In comparison to non-specific control (NS), *FBXO45* depletion increased cell proliferation (~4.2-fold, P = 0.0008) and colony formation in BJAB cells (4.3-fold, P = 0.0002) (Supplementary Fig. S6A-S6C). Similarly, *FBXO45* depletion increased cell proliferation (2.2-fold, P = 0.049) and colony formation in FL518 cells (3.0-fold, P = 0.01) (Supplementary Fig. S6D and S6E). Additionally, co-silencing of *ARHGEF2* and *FBXO45* reverted colony formation promoted by *FBXO45* loss (BJAB, 1.6-fold, P = 0.0003; FL518, 1.2-fold P = 0.01), suggesting that GEF-H1 stabilization resulting from *FBXO45* depletion is partly responsible for the observed phenotype (Supplementary Fig. S6C and S6E). As expected (34), knockdown of *ARHGEF2* alone reduced the number of colonies compared to *NS* shRNA controls (BJAB, 0.4-fold, p=0.019; FL518, 0.2-fold, p=0.01; [Supplementary Fig. S6C and S6E]).

To evaluate the contribution of GEF-H1 in FBXO45-mediated lymphomagenesis, tumor growth and survival was assessed in xenografts of FL518 lymphoma cells stably expressing *NS shRNA* ($FL518^{NS\ shRNA}$), *FBXO45 shRNA* ($FL518^{FBXO45\ shRNA}$), *ARHGEF2 shRNA* ($FL518^{ARHGEF2}$

^{shRNA}) or *FBXO45 shRNA and ARHGEF2 shRNA* (FL518$^{FBXO45\ shRNA,\ ARHGEF2\ shRNA}$). Consistent with our previous *in vitro* results, we observed a significant increase in tumor volumes in FL518$^{FBXO45\ shRNA}$ xenografts compared to FL518$^{NS\ shRNA}$ ($P<0.05$). Mice xenografted with FL518$^{FBXO45\ shRNA,\ ARHGEF2\ shRNA}$ showed reduced tumor volume as compared to FL518$^{FBXO45\ shRNA}$ xenografts. Mice xenografted with FL518$^{ARHGEF2\ shRNA}$ cells did not develop palpable tumors (Supplementary Fig. S6F). Whereas most mice harboring FL518$^{NS\ shRNA}$ xenografts were alive beyond 25 days, all mice xenografted with FL518$^{FBXO45\ shRNA}$ cells exhibited significant decrease in survival ($P<0.016$) and did not survive beyond 16 days. All mice xenografted with FL518$^{ARHGEF2\ shRNA}$ survived without palpable tumor growth until the end of the experiment. Importantly, mice xenografted with FL518$^{FBXO45\ shRNA,\ ARHGEF2\ shRNA}$ showed increased survival (median survival 22.5 days) indicating partial rescue of the *FBXO45* depletion phenotype (Supplementary Fig. S6G). Taken together, these results indicate that *FBXO45* loss promotes lymphoma growth *in vivo*, and this phenotype is significantly ameliorated by GEF-H1 depletion.

Abnormal expansion of the GCB-compartment is reverted by co-deletion of *Arhgef2*

To further analyze the molecular mechanism involved in FBXO45-mediated regulation of GCB-cell expansion, we generated transgenic mice in which *Arhgef2* (the gene that encodes GEF-H1) is specifically deleted in GCB-cells (*Cγ1Cre*$^{tg/+}$-*Arhgef2*$^{fl/fl}$). We further generated double knockout mice targeting both *Fbxo45* and *Arhgef2* (*Cγ1Cre*$^{tg/+}$-*Fbxo45*$^{fl/fl}$*, ;Arhgef2*$^{fl/fl}$) by crossing mice bearing genotype *Cγ1Cre*$^{tg/+}$-*Fbxo45*$^{fl/fl}$ with mice carrying genotype *Cγ1Cre*$^{tg/+}$-*Arhgef2*$^{fl/fl}$ (Fig. 4A). Splenic GCB-cells from mice were analyzed 10 days after immunization with SRBC as stated previously using CD95 and PNA staining. SRBC-immunized *Cγ1Cre*$^{tg/+}$-*Fbxo45*$^{fl/fl}$ mice demonstrated median 1.7-fold increase (6.11%, $P=0.001$) in the percentage of GCB-cells as compared to *Cγ1Cre*$^{tg/+}$-*Fbxo45*$^{+/+}$ (4.42%). Interestingly, the percentage of GCB-cells was significantly reduced in *Cγ1Cre*$^{tg/+}$-*Fbxo45*$^{fl/fl}$*;Arhgef2*$^{fl/fl}$ double knockout (3.80%, $P = 0.029$). The percentage of GCB-cells was significantly reduced in *Cγ1Cre*$^{tg/+}$-*Arhgef2*$^{fl/fl}$ mice (1.36%, $P = 0.011$) as well. (Fig. 4B). These observations were corroborated using CD95 and GL7 staining (Supplementary Fig. S7A and S7B). In summary, flow cytometric analyses demonstrated a dose-dependent increase in the proportion of GCB-cells upon loss of *Fbxo45* in GCB-cells (38% increase in PNA+ GCB-cells in *Cγ1Cre*$^{tg/+}$-*Fbxo45*$^{fl/fl}$ mice, $P<0.01$ (Fig. 4C), and 62% increase in GL7+ GCB-cells in *Cγ1Cre*$^{tg/+}$-*Fbxo45*$^{fl/fl}$ mice, $p<0.01$ [Supplementary Fig. S7B]. Importantly, in comparison to the *Cγ1Cre*$^{tg/+}$-*Fbxo45*$^{fl/fl}$ mice, *Cγ1Cre*$^{tg/+}$-

Fbxo45$^{fl/fl}$;*Arhgef2*$^{fl/fl}$ double knockout mice displayed a significant decrease (P<0.01) in GCB-cell formation (Fig. 4C; Supplementary Fig. S7B). Strikingly, complete ablation of GEF-H1 in *Cγ1Cre*$^{tg/+}$-*Arhgef2*$^{fl/fl}$ mice resulted in a 31% decrease in the frequency of GCB-cells as compared to WT littermate controls (p<0.05). Taken together, these studies provide strong genetic evidence to suggest that FBXO45 controls the GCB cell compartment through a regulatory axis involving GEF-H1.

Arhgef2 co-deletion reverts lymphomagenesis in _Fbxo45_ knockout mice

Importantly, GCB-cell lymphomagenesis caused by loss of *Fbxo45* was abrogated by double knockout of *Fbxo45* and *Arhgef2* (Fig. 4D). Specifically, 0/20 (0%) of *Cγ1Cre*$^{tg/+}$-*Fbxo45*$^{+/+}$ (WT) mice exhibited lymphoma on necropsy or gross examination. By comparison, 20/20 (100%) of *Cγ1Cre*$^{tg/+}$-*Fbxo45*$^{fl/fl}$ (*Fbxo45* homozygous KO) mice exhibited gross evidence of lymphomas in the spleen. In this regard, only 1/11 (9%) of *Cγ1Cre*$^{tg/+}$-*Fbxo45*$^{fl/fl}$;*Arhgef2*$^{fl/fl}$ (double homozygous *Fbxo45* and *Arhgef2*) knockout mice exhibited macroscopic evidence of lymphoma. Microscopic examination of spleens from WT mice revealed normal follicular architecture. *Cγ1Cre*$^{tg/+}$-*Fbxo45*$^{fl/fl}$ mice demonstrated effacement of splenic architecture by diffuse proliferation of large transformed lymphoid cells (Fig. 4E, middle panel). In all but 1/11 cases, double homozygous knockouts of *Fbxo45* and *Arhgef2* revealed a nodular splenic architecture without effacement or lymphoma (Fig. 4E). These results demonstrate that the *Fbxo45-Arhgef2* axis is functionally relevant in GCB-cell formation and lymphomagenesis *in vivo*.

Whole genome sequencing reveals mutually exclusive copy number loss of _FBXO45_ and gains of _ARHGEF2_ in primary human B-cell lymphomas

To investigate whether genomic alterations occur in *FBXO45* and/or its substrate GEF-H1, we analyzed whole genome sequencing (WGS) data from a total of 404 cases of lymphoma from two independent cohorts; namely the British Columbia Cancer Agency (BCCA; n=238) and the International Cancer Genome Consortium-Molecular Mechanisms of Malignant Lymphomas (ICGC MMML; n=166). Advantageously, both cohorts employed sequencing of tumor-normal pairs facilitating accurate and sensitive detection of somatic variants and copy number variations.

In contrast to targeted sequencing assays which cover less than 0.5% of the genome and exome sequencing which interrogates only ~1.5% of the genome, WGS permits interrogation of all structural alterations in the entire genome including large structural variations (SV), insertion-deletions, single nucleotide variations, translocations and copy number alterations (CNA), hence providing the opportunity to identify numerous genomic alterations in cancer that are undetectable by targeted or exome sequencing. Accordingly, to capture the entire spectrum of genomic structural alterations and copy number changes affecting *FBXO45* and *ARHGEF2*, we analyzed WGS data on FLs (n=209) and DLBCLs (n=195) from the BCCA and ICGC cohorts (Supplementary Fig. S8A-S8C and Supplementary Table S4). The SV affecting the *FBXO45* and *ARHGEF2* loci were defined as intrachromosomal events with breakpoints within 1 Mbp region from the gene of interest.

Among this cohort of patients, both *FBXO45* and *ARHGEF2* were affected by either copy number alterations or structural variations. The overall frequency of copy number loss affecting *FBXO45* was 2.7% (n = 11/404 of samples), while *ARHGEF2* copy number gains were observed in 32.7% (n = 132/404 of samples). Our studies showed that copy number variations are the main mechanism of genomic alteration of *FBXO45* and *ARHGEF2* in B-cell lymphoma (Supplementary Table S4).

Further, we investigated the distribution of *FBXO45* and *ARHGEF2* alterations in the subgroups of FL and DLBCL. WGS analysis of the combined BCCA and ICGC cohorts (40) revealed that the aggregate frequencies of *FBXO45* deletions were (5/209; 2.39%) in FL and (6/195; 3.08%) in *de novo* DLBCL (Supplementary Fig. S8A, and Supplementary Table S4). By comparison, *ARHGEF2* gains were observed in 50/209 cases; (24%) of FL and 82/195 cases (42%) of DLBCL. *ARHGEF2* gains were also mutually exclusive with the *FBXO45* deletions in both FL and DLBCL (p= 0.02 and p= 0.03 respectively, Comet exact test; Supplementary Fig. S8B).

To further evaluate the gains of *ARHGEF2* and loss of *FBXO45* genes observed in our WGS analyses, we performed analysis using the GISTIC2 on the FL and DLBCL combined cohorts (Supplementary Table S4). We observed a deletional segment with limits that included the *ARHGEF2* gene (Supplementary Table S4) (40). We next evaluated *ARHGEF2* copy number gains and RNA expression and observed a significant correlation between *ARHGEF2* copy number gains and high levels of RNA expression from RNA sequencing in *de novo* DLBCLs (p = 1.8e-05), and correlated trend in FLs (p = 0.066) (Supplementary Fig. S8D). For

FBXO45, similar GISTIC2 analysis and assessment of corresponding changes in RNA expression did not reveal statistically significant correlation between genomic loss of *FBXO45* and reduced transcript expression.

To further substantiate our observations of copy number alterations in *FBXO45* and *ARHGEF2* identified by WGS, we performed fluorescence *in situ* hybridization (FISH) which corroborated WGS observations of *FBXO45* deletion and *ARHGEF2* gains in primary human lymphoma (Supplementary Fig. S8E, S8F and Supplementary Table S5). Taken together, these data implicate recurrent genetic alterations targeting *FBXO45* and *ARHGEF2* in the most common subtypes of human B-cell lymphomas; (DLBCL and FL).

We next sought to determine the distribution of *FBXO45* and *ARHGEF2* copy number alterations using the LymphGen classifier for categorization into genetic subgroups of DLBCL (41). Among the 11 cases carrying *FBXO45* genomic loss, 4/11 (36.36%) were classified as EZB, 4/11 (36.36%) were classified as other, 2/11 (18.2%) were classified within the BN2 subtype, and 1/11 (9.1%) classified as ST2 subtype. No cases (0/11) were assigned to BN2 COMP, EZB-COMP, MCD or MCD-COMP subtypes.

Stratifying the DLBCLs (BC and ICGC cohort) into genetic subgroups showed an over-representation of *ARHGEF2* gains in BN2 (n = 19/42, 45%) and ST2 (n = 10/18, 56%) relative to EZB (n = 58/231, 25%) (Supplementary Table S4). Taken together, these data indicate that cases carrying *FBXO45* deletions fall most frequently into the EZB and “other” categories, while DLBCLs with *ARHGEF2* gains are observed more frequently in the ST2, BN2, and EZB subtypes, although also seen at variable frequencies across all genetic subtypes (Supplementary Fig. S8C and Supplementary Table S4).

GEF-H1 S644 is critical for interaction with FBXO45 and GEF-H1 polyubiquitylation

F-box proteins are known to recognize their substrates via specific degradation motifs (or degrons) within the substrates, and substrate binding may be regulated by post-translational modifications such as phosphorylation (42). To determine whether the interaction between FBXO45 and GEF-H1 is phosphorylation-dependent, we performed co-immunoprecipitation experiments in the presence of lambda phosphatase (λ-PPase), with and without a phosphatase inhibitor. Treatment with λ-PPase, but not λ-PPase in the presence of the phosphatase inhibitor, diminished FBXO45 interaction with GEF-H1 (Fig. 5A). To determine the sequence recognition motif in GEF-H1 required for binding FBXO45, we generated a series of GEF-H1 deletion

mutants and performed binding experiments to systematically map the FBXO45 recognition motif in GEF-H1. These experiments revealed that the binding motif for FBXO45 resides between amino acids 622 and 672 of GEF-H1 (Fig. 5B-5C) containing a conserved $E^{643}SLE^{646}$ motif. Since the interaction is dependent on phosphorylation of GEF-H1, we generated a substitution mutation of S644 which is a conserved amino acid residue in this fragment that can potentially be phosphorylated. We also generated a mutant of an adjacent serine residue (S642) which is not conserved across different species (Fig. 5D). The GEF-H1 S644A mutant did not associate with FBXO45 in reciprocal immunoprecipitation experiments while the GEF-H1 S642A mutant maintained the interaction (Fig. 5E and Supplementary Fig S9A). We further demonstrated that the GEF-H1 S644A mutant failed to interact with FBXO45 in BJAB cells (Fig. 5F). Moreover, *in vitro* ubiquitylation assays revealed that FBXO45 promotes ubiquitylation of wild-type GEF-H1, but not GEF-H1 S644A (Fig. 5G). Taken together, these data strongly indicate that FBXO45 mediates ubiquitin-mediated proteasomal degradation of GEF-H1.

GEF-H1 S644A mutation promotes B-cell proliferation, colony formation, MAPK signaling and lymphomagenesis in xenograft model

Next, we sought to investigate the effect of the degradation-resistant GEF-H1 S644A mutant on B-cell lymphomagenesis. To this end, we stably expressed doxycycline-inducible GEF-H1 WT and the degradation resistant GEF-H1 S644A mutant in BJAB cells (Supplementary Fig. S9B upper panel). We observed that expression of GEF-H1 S644A prolongs GEF-H1 half-life and pERK1/2 levels (Supplementary Fig. S9B lower panel), and promotes B-cell proliferation (Supplementary Fig. S9C) and colony formation ($P<0.05$) (Supplementary Fig. S9D) compared to GEF-H1 WT. Similarly, constitutive expression of V5-tagged GEF-H1 S644A mutant in FL518 cells prolongs GEF-H1 half-life, promote B-cell proliferation and colony formation compared to GEF-H1 WT (Supplementary Fig S9E, S9F and S9G).

To investigate the *in vivo* tumorigenic potential of the GEF-H1 S644A mutant, we established murine xenografts of FL518 cells stably expressing vector control (n = 5), GEF-H1 WT (n = 5) and GEF-H1 S644A mutant (n = 5) by subcutaneous injection of 1 X 10^6 cells into NOD.CB-*Igh-l*^{b} *GbmsTAC-Prkdc*^{scid}*-Lyst*^{bg}*N7* (SCID-BEIGE) mice and assessed tumor growth and survival over time. Mice injected with cells expressing $FL518^{GEF\text{-}H1\ S644A}$ mutant showed increased tumor growth when compared with the $FL518^{GEF\text{-}H1\ WT}$ and $FL518^{EV}$ (EV= empty

vector) cells (Supplementary Fig. S9H) (P<0.0001). Mice xenografted with FL518^{EV} were alive beyond 25 days. By contrast, mice xenografted with FL518$^{GEF\text{-}H1\ WT}$ and FL518$^{GEF\text{-}H1\ S644A}$ exhibited significant decrease in survival (median survival was 21 days for GEF-H1 WT and 13 days for GEF-H1 S644A; EV vs GEF-H1 S644A; P<0.0001). In this regard, mice harboring FL518$^{GEF\text{-}H1\ S644A}$ cells did not survive beyond 16 days (Supplementary Fig. S9I). By comparison, animals xenografted with FL518$^{GEF\text{-}H1\ WT}$ survived for $\geq$20 days which was also significantly longer than animals xenografted with FL518$^{GEF\text{-}H1\ S644A}$ mutant (GEF-H1 WT vs GEF-H1 S644A; P=0.0014), but not significantly less than animals xenografted with FL518^{EV} (EV vs GEF-H1 WT; P=0.0562) (Supplementary Fig. S9I). These results indicate that expression of the degradation-resistant GEF-H1 S644A potentiates tumor growth and aggressiveness *in vivo*.

In vivo transgenic knock-in of _Arhgef2_ S644A results in disseminated B-cell lymphoma

Having observed that the degradation-resistant GEF-H1 S644A mutant promotes B-cell lymphoma in a xenograft model, we sought to investigate the lymphomagenic potential of defective GEF-H1 degradation by generating a transgenic *Arhgef2* S644A knock-in mouse model using CRISPR-Cas9-mediated genomic editing. We generated the following cohort of genotypes; *Arhgef2*-wild type (*Arhgef2* S644 WT), *Arhgef2* S644A-heterozygous knock-in (*Arhgef2* S644A$^{+/-}$) and *Arhgef2*-homozygous knock-in (*Arhgef2* S644A$^{+/+}$) (Fig. 6A). After Sanger sequencing knock-in validation (Fig. 6B), we purified splenic B-cells from the *Arhgef2* S644 WT and *Arhgef2* S644A$^{+/+}$ mice and subjected them to cycloheximide and monitored protein stability over time. Splenic B-cells from *Arhgef2* S644A$^{+/+}$ mice demonstrate increased stability of GEF-H1 as compared to *Arhgef2* S644 WT (Fig. 6C and 6D). Notably, disseminated B-cell lymphomas at various anatomic locations were detected in the *Arhgef2* S644A$^{+/-}$ (40%) and *Arhgef2* S644A$^{+/+}$ (50%) mice while only reactive GCs were observed in *Arhgef2* S644 WT mice (Fig. 6E and 6F). Necropsy revealed enlarged spleens and livers in *Arhgef2* S644A$^{+/+}$ mice as compared to WT littermates (Fig. 6F). In basal and acute stimulation contexts, using sheep RBCs, we did not observe significant differences in the distribution of B-cell, T-cell, GCB-cell, dark zone (DZ)-cells, light zone (LZ)-cells or DZ/LZ ratio between *Arhgef2* S644 WT (n=5) and *Arhgef2* S644A$^{+/+}$ mice (n=5) by flow cytometry analysis of 4-6 week old mice (Supplementary Fig. S9J). However, when we evaluated aged animals, we observed lymphomas with positive immunohistochemical reactivity for PNA in spleen, liver and intestine suggesting germinal center derived B-cell lymphoma only in the Arhgef2 S644A mutant mice (Fig. 6G). Histological

examination confirmed B-cell lymphoma in the liver, and intestine with expansion of follicles, increased CD19+ and PNA+ B-cells in *Arhgef2* S644A$^{+/-}$ and *Arhgef2* S644A$^{+/+}$ mice (Fig. 6G). Intestinal lymphoma observed in *Arhgef2* S644A$^{+/+}$ mice exhibited diffuse sheets of atypical medium-sized lymphocytes infiltrating the wall of the bowel, which were CD19+, PNA- representing diffuse B-cell lymphoma. Livers of *Arhgef2* S644A$^{+/+}$ mice also showed extensive infiltration by large pleomorphic lymphoma cells with blastic nuclei and partial PNA+, CD19+ aggressive B-cell lymphoma (Fig. 6G). Next generation sequencing of the immunoglobulin heavy chain gene using DNA extracted from tumor of *Arhgef2* S644A$^{+/+}$ mice revealed prominent monoclonal population (Fig. 6H).

Taken together, *in vivo* knock-in of *Arhgef2* S644A leads to high penetrance (40-50%) development of B-cell lymphoma. Collectively, these observations support an oncogenic function of degradation-resistant GEF-H1 S644A.

FBXO45 **deficiency sensitizes B-cell lymphoma to MAPK pathway inhibition** ***in vitro*** **and** ***in vivo***

GEF-H1 has been demonstrated to promote MAPK signaling (34). Accordingly, along with its increased stability, the GEF-H1 S644A mutant increased MAPK signaling observed by increased and prolonged pERK1/2 levels relative to GEF-H1 WT-expressing cells (Supplementary Fig. S9B). Further, *ARHGEF2* knockdown in BJAB cells resulted in downregulation of pERK1/2 signaling and levels of active RhoA (Supplementary Fig. S10A). We re-expressed inducible GEF-H1 WT or GEF-H1 S644A mutant in *ARHGEF2* knockdown BJAB cells. Western blot analysis showed that re-expression of GEF-H1 S644A mutant upregulated pERK1/2 levels and active RhoA levels compared to GEF-H1 WT expression (Supplementary Fig. S10B). Further, we observed that cells expressing GEF-H1 S644A mutant exhibit increased rate of cell proliferation compared to GEF-H1 WT expressing cells (Supplementary Fig. S10C). To investigate the role of FBXO45 in GEF-H1-mediated cell proliferation, we co-expressed FLAG-tagged FBXO45 with FLAG-tagged inducible GEF-H1 WT or GEF-H1 S644 mutant (Supplementary Fig. S10D). We observed that the expression of FBXO45 reduced the rate of proliferation in cells expressing GEF-H1 WT, but not that in GEF-H1 S644A mutant expressing cells (Supplementary Fig. S10E and S10F).

Given our observation that FBXO45 regulates GEF-H1 degradation and that degradation-resistant GEF-H1 S644A mutant increases and prolongs MAPK signaling

(Supplementary Fig. S9B), we reasoned that loss of FBXO45 may promote MAPK signaling. Cycloheximide pulse-chase in BJAB and FL518 isogenic cell lines expressing *FBXO45* shRNA or *NS* shRNA shows that *FBXO45* knockdown increased not only basal levels of pERK1/2 but also prolonged pERK1/2 signaling (Supplementary Fig. S11A and S11B). Further, we observed that while knockdown of *ARHGEF2* reduced pERK1/2 levels (Supplementary Fig. S10A and S11C), *FBXO45* and *ARHGEF2* double knockdown partially rescued pERK1/2 signaling (Supplementary Fig. S11C). Cycloheximide pulse-chase experiments in BJAB cells with CRISPR-Cas9-mediated *FBXO45* KO (Supplementary Fig. S5G) revealed marked prolongation of the half-life of GEF-H1 and persistence of ERK1/2 phosphorylation, without affecting ERK1/2 total levels (Fig. 7A). Importantly, the cycloheximide pulse-chase experiments in GCB-cells purified from *Cγ1Cre$^{tg/+}$-Fbxo45$^{+/+}$* or *Cγ1Cre$^{tg/+}$-Fbxo45$^{fl/fl}$* showed increased stabilization of GEF-H1 and persistent pERK1/2 detection at 4 hours (Supplementary Fig S11D).

Based on our observation of hyperphosphorylation of pERK1/2 consequent to FBXO45 loss, we sought to investigate whether FBXO45 deficiency conferred differential sensitivity of B-cell lymphoma to MAPK inhibitors. Thus, we investigated the functional consequence of pharmacological inhibition of the MAPK pathway using the FDA-approved selective MEK1/2 inhibitor, Trametinib (GSK1120212). Trametinib treatment of isogenic B-cell lymphoma derived cell line, BJAB, with inducible CRISPR-Cas9-mediated KO of *FBXO45* (i.e., iBJAB *KO*; i=doxycycline inducible Cas9 expression) demonstrated a marked dose- and time-dependent decrease in cell viability (Supplementary Fig. S12A and S12B). Significant decrease in cell viability was observed with 30 μM Trametinib as early as 24 hours (76.86 ± 4.12 % of control; $P<0.05$), at 48 hours (63.76 ± 2.37 %; $P<0.05$) and at 72 hours (56.25 ± 2.48 %; $P<0.05$) for iBJAB *FBXO45 KO* cells. Importantly, treatment with 30 μM Trametinib induced apoptosis with increased lymphoma-cell death in an autologous coculture system using cells from *Cγ1Cre$^{tg/+}$-Fbxo45$^{fl/fl}$* (HOM) splenic cells compared to *Cγ1Cre$^{tg/+}$-Fbxo45$^{+/+}$* (WT) splenic cells (Supplementary Fig. S12C). Further, knockdown of MEK1, MEK2 or both significantly ($p=0.003$) reduced proliferation of *FBXO45* KO iBJAB cells compared to isogenic *FBXO45* WT iBJAB cells (Supplementary Fig. S12D).

Given the hyperactivation of ERK1/2 in *FBXO45 KO* cells and increased susceptibility of FBXO45-deficient cells to the MEK1/2 inhibition (Fig. 7A-7B and Supplementary S11 and S12A-S12D), we sought to investigate the effect of *FBXO45* loss on sensitivity to pharmacologic blockade using Trametinib *in vivo*. Therefore, we tested the efficacy of Trametinib in inhibiting

the growth of iBJAB-*FBXO45 KO* B-cells xenografted in NSG mice. Our studies show significant (39%, P<0.0001) inhibition of lymphoma growth by Trametinib in *FBXO45* KO cells (tumor volume 1397.19 ± 90.06 mm^3; Day 25) as compared to their isogenic WT (tumor volume 2268.83 ± 204.20 mm^3; Day 25) counterparts. Fig. 7C shows that tumors from mice carrying *FBXO45* KO cells were significantly (P<0.0001) smaller than those observed in tumors from *FBXO45* WT. Fig. 7D shows mice bearing tumors illuminated by GFP and captured by *in vivo* fluorescence imaging as well as tumors extracted from mice on Day 25 for size evaluation. We further tested the efficacy of Trametinib-mediated inhibition of tumor growth in DLBCL using *in-vivo* bioluminescence imaging. In this regard, we transduced transformed DLBCL cells, FL518, with the luciferase (Luc)-EGFP gene. These cells were further transduced with non-specific shRNA (*NS*) ($FL518^{GFP\text{-}Luciferase,\ NS\ shRNA}$) or shRNA targeting FBXO45 (*FBXO45*) ($FL518^{GFP\text{-}Luciferase,\ FBXO45\ shRNA}$). Flow cytometric analysis of the isogenic cell line $FL518^{GFP\text{-}Luciferase,\ FBXO45\ shRNA}$ showed increased cell death compared to $FL518^{GFP\text{-}Luciferase,\ NS\ shRNA}$ following Trametinib treatment *in vitro* as measured by Annexin V+ PI+ staining (Supplementary Fig. S12E). Further, the bioluminescence imaging analysis of xenografts of $FL518^{GFP\text{-}Luciferase,\ FBXO45\ shRNA}$ in mice that received Trametinib exhibited significant reduction in tumor growth as compared to $FL518^{GFP\text{-}Luciferase,\ NS\ shRNA}$ mice (Fig. 7E and 7F). Kaplan-Meier curves show that the median survival of mice xenografted with $FL518^{GFP\text{-}Luciferase,\ NS\ shRNA}$ with Trametinib was 28.5 days and 23 days with vehicle alone. Significantly, Trametinib treatment of mice xenografted with $FL518^{GFP\text{-}Luciferase,\ FBXO45\ shRNA}$ showed an increased median survival of 33 days and 19 days with vehicle alone (P≥0.0001) (Fig. 7G). Additionally, Trametinib treatment also reduced the viability of BJAB cells overexpressing inducible GEF-H1 WT much akin to increased copy number observed in our clinical studies and show elevated apoptosis observed by increased cleaved caspase 3 levels (Supplementary Fig. 12F).

Taken together, these results indicate that FBXO45 loss promotes deregulated and prolonged MAPK pathway activation and that tumors lacking FBXO45 are sensitive to MAPK pathway inhibition.

DISCUSSION

Our integrated structural and functional genomic studies and quantitative proteomics led to the identification of a previously unappreciated FBXO45-GEF-H1 pathway that is involved in

the regulation of GC formation and frequently disrupted in the two most common subtypes of human lymphomas; FL and DLBCL, which collectively account for 50-70% of human lymphomas (17,43-45). Our whole genome sequencing analysis studies revealed that genomic alterations targeting *FBXO45* (copy number loss) and *ARHGEF2* (copy number gains) are recurrent in GCB-cell lymphomas. The biological role of FBXO45 as a tumor suppressor is further highlighted by the remarkable 100% penetrance of widely disseminated GCB-cell lymphoma development in conditionally targeted homozygous *Fbxo45*-deficient mice. Double knockout of *Fbxo45* and *Arhgef2 in vivo* significantly abrogated lymphomagenesis. Similarly, failure to degrade GEF-H1 following FBXO45 depletion or expression of the degradation-resistant GEF-H1 S644A mutant in human B-lymphoma cell lines promotes lymphoma growth in xenograft models *in vivo*. Further, transgenic expression of the degradation resistant GEF-H1 S644A mutant results in the development of disseminated B-cell lymphoma with 50% frequency. Physiologically, we observed that loss of FBXO45 increases GCB-cells in a dose-dependent manner and hyperactivates RhoA and MAPK signaling, and simultaneous loss of *Fbxo45* and *Arhgef2* partially rescues the phenotype. Significantly, we observed that FBXO45 loss results in enhanced sensitivity to pharmacologic blockade of the MAPK pathway, suggesting that antagonism of this pathway could represent a novel therapeutic opportunity in the significant number of lymphomas harboring alterations in the FBXO45-GEF-H1 axis.

The F-box family of E3 ubiquitin ligases are increasingly being recognized for their role in diverse biological pathways including cell growth, differentiation and cancer (46-48). With regard to B-cell lymphomas, FBXO11 has been implicated in the pathogenesis of DLBCL through degradation of BCL6 (49-51). However, no functions have been described for FBXO45 in the hematopoietic or immune system. While a putative role in cancer as an oncogene has been suggested by previous studies, these observations have not been substantiated by rigorous studies using *in vivo* genetic ablation. In this regard, FBXO45 was suggested to exhibit a putative oncogenic role through degradation of substrates including tumor-suppressor p73 (52) and the proapoptotic protein PAR4 (53). Additionally, ectopic expression of FBXO45 has been reported to enhance tumor growth in pancreatic cancer (54), and elevated levels of Fbxo45 have been associated with liver tumorigenesis (55). Here, we demonstrate a novel and unanticipated tumor suppressor role for FBXO45 in B-cell lymphoma. Mechanistically, we show that GEF-H1 is a substrate of the FBXO45 E3 ubiquitin ligase and failure to degrade GEF-H1 by

Fbxo45-deficiency or expression of degradation-resistant GEF-H1 promotes B cell lymphomagenesis *in vivo*.

Recent studies show that GEF-H1 is an important mediator of MAPK activation, cellular growth and transformation (34). We show here that either failure to degrade GEF-H1 due to FBXO45 loss, or expression of a degradation-resistant GEF-H1 mutant results in hyperactivation of MAPK signaling to promote B-cell oncogenesis. We further show that conditional targeting of *Arhgef2* in GCB cells rescues the lymphomagenic phenotype resulting from *Fbxo45* deficiency. Moreover, we demonstrate that pharmacological antagonism of MAPK signaling preferentially inhibits the growth of B-cell lymphomas lacking FBXO45. The availability of approved selective inhibitors targeting the MAPK signaling may thus represent options for patients with lymphomas harboring abnormalities in this pathway.

In summary, our findings define a novel FBXO45-GEF-H1 signaling axis (Supplementary Fig. S13) which plays an important role in germinal center formation and DLBCL and FL pathogenesis. Our studies suggest that novel therapeutic strategies targeting GEF-H1 or MAPK may be considerations for cancers exhibiting FBXO45 deficiency. Overall, our studies highlight the promising prospects of functional proteogenomic approaches to elucidate novel pathways and mechanisms that may be exploited for discovery of targeted, potentially less toxic and more efficacious therapies for major cancers**.**

Authors' Contribution

K.S.J.E.J. and M.S.L. conceived and coordinated the study, analyzed data, oversaw the project. K.S.J.E.J., M.S.L. A.A.S. and X.C. wrote the manuscript. A.A.S., X.C., K.M., R. W., R.K.,H-C. L., O.O., J.S.V.A., J.W., C.M.H., R.R.C, P.S. and C.L. performed experiments and analyzed data. R.S. and L.M.S. designed experiments and analyzed data. M.P.C., D.A., B.G., D.K., and J.K. analyzed immunophenotypic and RNA Sequencing data. T.D.R. designed and performed the CRISPR strategy for generation of the *Arhgef2* knock-in mouse. V.P. and M.S.L. provided clinical material. N.G.B., M.S.L. and K.S.J.E.J. analyzed histologic and immunophenotypic studies. R.R. provided critical input and reagents. M.P. generated critical reagents and analyzed data. M.M.L., J.S., M.S., R.S. and L.M.S. analyzed genomic data. V.B. and O.O. and K.P.C. performed mass spectrometry experiments. A.A.S., X.C., R.W., R.R.C., R.K., M.S.L., and K.S.J.E.J. generated figures and display items. All authors discussed the results and commented on the manuscript.

Acknowledgments

We thank Dr. Zhaosheng Lin for quantitative proteomics experiments on primary lymphoma cells. We thank Dr. Damian Fermin for NSAF analysis of MS/MS data. We thank Dr. Rabea Wagener for her assistance with compilation of genomic data and Dr. Bryan Betz for input for FISH probe design. We thank Dr. Vania Aikawa and Susan Nedumakel for technical assistance with FISH studies. We thank Loni Pickle and Geoffrey M. Lowman from Thermo Fisher Scientific for assistance with mouse BCR IGH SR assays. We thank Dr. Vijendra Ramlall for generating illustrations representing the results of immunoglobulin sequencing by NGS. We thank Dr. Veronica Mendoza-Reinoso for assistance with establishment of lymphoma xenografts and Dr. Delphine Rolland for helpful discussions and logistical facilitation of the project. We thank Xia Yang, Kevin Dennis for assistance with husbandry and genotyping of transgenic mice. We thank Faith Key for her assistance with immunohistochemistry. We are grateful to Dr. Eline T. Luning-Prak and Wenzhao Meng of the Human Immunology Core at University of Pennsylvania for assistance with clonotypic analysis. The members of the ICGC MMML-Seq Consortium are gratefully acknowledged. This research was supported by Cycle for Survival and funded in part through the NIH/NCI Cancer Center Support Grant P30 CA008748. This work was also supported by National Institutes of Health grant R01CA231021 to KSJEJ and National Institutes of Health grant R35 GM136250 to MP. MP is an investigator with the Howard Hughes Medical Institute. This work was also supported by a Terry Fox New Investigator Award (No. 1043) and by an operating grant from the Canadian Institutes for Health Research and a New Investigator Award from the Canadian Institutes for Health Research to R.D.M. R.S. and the team are supported by International Cancer Genome Consortium-Molecular Mechanisms in Malignant lymphomas-Sequencing (ICGC-MMML-Seq;01KU1002A-J) and International Cancer Genome Consortium DE-Mining (01KU1505G and 01KU1505E) awards.

METHODS

ICAT labeling of proteins and 3-D LC-MS/MS

ICAT (isotope-coded affinity tag) labeling and 3-D LC were performed as described previously (56) with some modifications (Supplementary Fig. S1). Equal amounts of protein (1 mg) in 800 µl of lysis buffer were taken for each sample (low-grade FL or transformed DLBCL). Proteins were reduced with 2.5 mM Tris [2-carboxyethyl] phosphine (Pierce) for 30 min at 37°C. ICAT

labeling was carried out by mixing 10 U of light (for low-grade FL) or heavy (transformed DLBCL) cleavable ICAT (Applied Biosystems, Foster City, CA) with respective protein samples following manufacturer's instruction and incubated for 90 min at 37°C. Labeled proteins were mixed and dialyzed against 250 ml of urea buffer (2 M urea, 10 mM Tris, pH 8.5) three times for 1 hour each at room temperature using the 3.5 kDa cut-off dialysis cassette (Pierce). The dialyzed protein mixtures were then diluted 2-fold with 10 mM Tris, pH 8.5, before digestion with 20 μg of modified trypsin (Promega, Madison, WI) overnight at 37 °C. The peptide mixture was then acidified to ≤pH 3.0 by adding TFA before loading onto the cation exchange column. The 3-D liquid chromatographic separation of peptides was carried out following these three steps. First, strong cation exchange chromatography using a 3.6-mm × 20-cm polysulfoethyl A column (Poly LC Inc., Columbia, MD) at a flow rate of 400 μl/min with 45 fractions collected (600 μl/fraction). A two-step linear buffer gradient was used: 5% buffer B and 95% buffer A to 25% buffer B and 75% buffer A for 50 min followed by 25% buffer B and 75% buffer A to 100% buffer B for 18 min (buffer A, 20 mM KH_2PO_4, 25% ACN, pH 3.0; buffer B, 350 mM KCl in buffer A, pH 3.0). Second, each fraction from the strong cation exchange chromatography was further purified by an ultralink monomeric avidin affinity cartridge (Applied Biosystems) to enrich only the cysteine-containing and ICAT-labeled peptides following the manufacturer's instructions. The eluted peptides were then dried and cleaved as instructed. Third, reverse-phase capillary chromatography was performed using an in-house packed C18 column (100 μm × 10 cm; Michrom BioResources, Inc., Auburn, CA) and an ACN gradient (57). The peptide samples were loaded and analyzed by a Surveyor LC linked to a LCQ DECA XP ion trap tandem mass spectrometer (ThermoFinnigan, San Jose, CA) using an automated method according to standard methods.

Protein identification and quantification for 3D-ICAT experiments

All MS/MS spectra were searched against the human protein database established by National Center for Biotechnology Information (NCBI) using the SEQUEST™ algorithm (58). Stable modification of cysteine was set as 227 and differential modification of cysteine set as 9. Proteins were identified based on the scoring criteria described previously (59) with the following modification: only identifications that fulfilled the following criteria were included in the search results, peptides of single, double, and triple charges should have respective cross correlation score (Xcor) ≥ 2.0, 2.0, and 3.0. Probability of identified proteins was analyzed using ProteinProphet™ (56). Protein quantification was performed using the XPRESS™ software

(ThermoFinnigan), which automatically calculates the relative abundance of light and heavy ICAT-labeled peptide as a ratio of light *versus* heavy (60).

RNA fluorescent In Situ Hybridization (RNA ISH) and immunofluorescent staining of reactive human tonsil

RNAscope ISH combined with anti-CD4 and anti-CD19 immunofluorescent staining was performed by the Laboratory of Comparative Pathology Core (MSKCC). The human RNAscope probe for *FBXO45* RNA ISH was synthetized by ACD (Hs-FBXO45, ACDBio, Ref. 312828) and used for immunofluorescent probing of paraffin-embedded reactive human tonsil using a Leica Bond RX platform and a Texas Red fluorophore. For CD4 and CD19 immunofluorescent co-staining, the conditions used are as follows: CD4 (1:1000 ON 4C; Abcam, ab133616), heat induced epitope retrieval in Tris-EDTA pH 9, Donkey Anti-Rabbit Alexa Fluor 488 secondary antibody (1:500, Invitrogen, A21206); CD19 (ready-to-use antibody, Leica, PA0843), Protocol F in the Leica Bond RX XIER ER2 (EDTA) for 20 min, Donkey Anti-Mouse Alexa Fluor 647 (1:500, Invitrogen, A31571). Nuclei were counterstained and visualized using DAPI fluorescent dye.

Antibodies for immunophenotyping, immunoprecipitation and western blotting

Antibodies used for western blotting and immunoprecipitation are GEF-H1; RRID: AB_2060032, pERK1/2; RRID: AB_331768, ERK1/2; RRID: AB_330744, RHOA; RRID: AB_10693922, FLAG; RRID: AB_262044, HA; RRID: AB_2314672, V5; RRID: AB_2537645, GAPDH; RRID: AB_561053, SKP1; RRID: AB_397887, MYCBP2; RRID: AB_1925230, Cullin1; RRID: AB_2533070, K48-PolyUbiquitin; RRID: AB_11213655, UBE1; RRID: AB_793598, UBE2D3; RRID: AB_3668663, PLK1; RRID: AB_2167409, β-Actin; RRID: AB_2223172, and α-Tubulin; RRID: AB_1904178. Antibodies used for flow cytometry are CD23 (B3B4)-PE; RRID: AB_10895122, CD23 (B3B4)–BV421; RRID: AB_2737898, Ter-119-PE; RRID: AB_10561843, GL7 antibody eFluor 660; RRID: AB_2574252, IgD (11-26.2a)-APC-Cy7; RRID: AB_10662544, CD4 (GK1.5)-PE-Cy7; RRID: AB_312706, Ter-119-PE-Cy7; RRID: AB_2137789, F4-80 (BM8)-PE-Cy7; RRID: AB_893490, B220 (RA3-6B2)-BV421; RRID: AB_10933424, Brilliant Violet 711™ anti-mouse CD19; RRID: AB_2565970, CD93 (AA4.1)-APC; RRID: AB_469466, CD21/35 (8D9)-PE-Cy7; RRID: AB_1518766, CD8α (53-6.7)-PE; RRID: AB_465530, CD8α (53-6.7)–PE-Cy7; RRID: AB_469584, CD19 (6D5)-APC-Cy5.5; RRID: AB_10373567, F4-80 (BM8)-PE; RRID: AB_10372666, B220 (RA3-6B2)-APC; RRID: AB_2621574, Peanut Agglutinin (PNA), Fluorescein; RRID: AB_2315097, PE Rat Anti-Mouse CD45R/B220; RRID: AB_10893353, PE-CyTM7 Hamster Anti-Mouse CD95; RRID: AB_396768.

Flow Cytometry for Immunophenotyping

Single-cell suspensions of murine splenocytes were resuspended in 1X RBC lysis buffer (BioLegend, Cat#420301) for 5 minutes on ice to remove red blood cells. Cell staining buffer (PBS with 5% FCS and 0.1% NaN3) were added to stop the lysis reaction. Cells were plated in a V-bottom 96-well plate at the density of 1 x 106 cells, followed by staining with Zombie Aqua (fixable viability dye) in PBS (1:100) for 15 minutes at 4°C in the dark. Cells were washed with cell staining buffer and incubated with CD16/32 (Fc block) and various cell surface markers (Supplementary Materials) in cell staining buffer (1:50) for 30 minutes at 4°C in the dark. Cells were washed with cell staining buffer and subsequently fixed using fixation buffer (BioLegend, Cat#420801) for 20 minutes at room temperature in the dark. Cells were washed and resuspended in cell staining buffer before analysis on flow cytometer. Compensation controls for each fluorochrome were processed the same way mentioned above except for staining with Zombie Aqua. Data were acquired using a BD LSRFortessa cytometer and analyzed using FlowJo v10 software.

Semi-quantitative determination of protein expression using immunohistochemistry staining and analysis

Semi-quantitative determination of germinal centre surface area and PNA expression was performed by Fiji (imageJ) (version 1.2; WS Rasband, National Institute of Health, Bethesda, MD) software and protocol- “https://bio-protocol.org/pdf/bio-protocol3465.pdf” using IHC images.

Cell Cycle Analysis

RBC lysis buffer treated single-cell suspension of murine splenocytes were plated at a density of 1 x 10^6 cells in a 12-well plate. Cell cycle phases were determined using BD Pharmingen™ APC BrdU Kit (BD Biosciences, Cat#552598) according to the manufacturer’s instructions. Cells were stained with GC B cell surface markers (Supplementary Materials) prior to BrdU pulse-labeling. Data were acquired using a BD LSRFortessa cytometer and analyzed using FlowJo v10 software. Cells were pre-gated on CD19+/B220+/CD95+/PNA+ population to identify GC B cells, followed by measurement of 7-AAD and BrdU incorporation.

Apoptosis Assay

RBC lysis buffer treated single-cell suspension of murine splenocytes were cultured at a density of 1 x 106 cells in a 12-well plate supplemented with anti-CD40 (1 µg/ml) (BD Biosciences, Cat#553721) and recombinant mouse IL-4 (100 ng/ml) (Gibco, Cat#214-14), followed by vehicle or Trametinib (30 µM; MedChemExpress, Cat#HY-10999) treatment for 72 hours. Live and

apoptotic cells were distinguished using Dead Cell Apoptosis Kits with Annexin V for Flow Cytometry (Invitrogen, Cat#V13241 & #A35110) according to the manufacturer's instructions. Cells were stained with GC B cell surface markers (Supplementary Materials) prior to Annexin V and propidium iodide (PI) staining. Data were acquired using a BD LSRFortessa cytometer and analyzed using FlowJo v10 software. Cells were pre-gated on CD19+/B220+/CD95+/PNA+ population to identify GC B cells, followed by Annexin V and PI measurement.

Strain-promoted azide-alkyne cycloaddition (SPAAC) Pulse-Chase

Cells were washed twice with methionine-free (Met-) DMEM to remove excess methionine then live-labelled (pulsed) at 37°C for 4 hours with 50 μM Click-iT L-azidohomoalanine (AHA; Invitrogen) in Met- DMEM supplemented with 10% FBX. AHA-labeled cells were then washed twice with Met+DMEM, and subsequently incubated in Met+ DMEM containing 10% FBS for 4, 8 and 16 hours at 37°C (Chase). For 0 hour time point, cells were collected on ice immediately following the Chase. Cell lysate prepared in RIPA buffer (Pierce #87787) were denatured in 1X Laemmli sample buffer (LSB) at 95°C for 10 minutes. For enrichment of AHA-labeled proteins, whole cell lysates (750 μg for each condition) were reacted with 10 μM Click-iT Biotin-DIBO (Invitrogen) for 1 hour at 21°C followed by 30 minutes incubation with Streptavidin-Agarose resin (Thermo-Scientific). After washing of the resin with RIPA buffer, bound protein was denatured with 1X LSB at 95°C for 10 minutes and protein levels were analysed by western blotting.

Protein synthesis measurement by L-Azidohomoalanine (AHA) labeling and flow cytometry

Cells were plated in a 6-well plate at the density of 1x106 cells, followed by starvation in methionine-free culture medium containing 10% FCS for 30 minutes. Cells were pulse-labeled with 1mM AHA or L-methionine (negative control) for 1 hour at 37°C with 5% CO2. Cells were washed with washing solution (1% BSA in PBS) and fixed in fixing solution (4% PFA in PBS) for 20 minutes at room temperature in the dark. Cells were washed with washing solution and permeabilized with permeabilization solution (1% BSA with 0.2% saponin in PBS) for 15 minutes at room temperature. Cells were washed with washing solution, followed by incubation with 100 µl of click reaction solution (1 µM Alexa Fluor 488 or 555 alkyne, 10 mM (+)-Sodium L-ascorbate and 2mM CuSO4 in PBS) for 30 minutes at room temperature in the dark. Cells were washed with permeabilization solution, followed by incubation with 100 µl of anti-phospho-Histone H3-Alexa Fluor 647 antibody (1:100 in washing solution) for 1 hour at 4°C in the dark.

Cells were washed with washing solution and resuspended in cell staining buffer. Data were acquired using a BD LSRFortessa cytometer and analyzed using FlowJo v10 software.

Cell lines and cell culture

DLBCL and transformed FL cell lines (BJAB; RRID: CVCL_5711, FL518; RRID: CVCL_IU41 and SUDHL6; RRID: CVCL_2206) were obtained as detailed in (61) and were cultured in RPMI supplemented with 10% fetal bovine serum (FBS), penicillin (100U/ml) and streptomycin (100 ug/ml). Cell lines were verified for identity using targeted resequencing of previously reported mutated gene. HEK293T cells; RRID: CVCL_0063 were cultured in Dulbecco's Modified Eagle Medium (Life Technologies) with 10% FBX, penicillin (100 U/ml) and streptomycin (100 ug/ml). All the cell lines were verified to be free from Mycoplasma contamination.

RNA extraction, cDNA synthesis and quantitative real-time PCR

Total RNA was extracted from DLBCL cell lines and primary mouse splenic B-cells using RNA purification kit (Qiagen) according to manufacturer"s instructions and measured using nanodrop (BioTek Synergy H1 Plate reader). Equal amounts of RNA were used to perform cDNA synthesis using the iScript cDNA Synthesis kit (BioRad # 1708891), according to the manufacturer's instructions. The Absolute QPCR SYBR green mix (ThermoFisher Scientific) was then used to amplify specific cDNA fragments in the 7300 Real Time PCR system (Applied Biosystems). Data were analyzed by the change-in-threshold ($2^{-\Delta\Delta C}{}_T$) method, using GAPDH as a house-keeping reference gene. The primers used for qRT-PCR are as follows: FBXO45: forward: 5' CTGTGGCAGTGATTGGAATTG 3', FBXO45 reverse 5' CAGGAACTCATATCCACGTTCA 3', GAPDH: forward 5' TGCACCACCAACTGCTTAGC 3', reverse 5' GGCATGGACTGTGGTCATGAG 3', ARHGEF2: forward 5' CCAATGTGGACGAGGGTATTTA 3', reverse 5' CTTGTCCAGGGTAGGAAAGATG 3', mArhgef2 forward 5' CTACCTCTCTGCTGACCCTGGCCTG 3', reverse 5' ACAGGAGACAAAACCAGTGGGGGTC 3'.

Transient transfection and lentivirus-mediated gene transfer and gene silencing

293T cells were transfected using Polyjet (Signagen). For lentiviral-mediated gene transduction, 293T cells were co-transfected with lentiviral construct and packaging vectors (Invitrogen). Virus-producing supernatant was harvested 48 hours after transfection and supplemented with polybrene and used to infect cells. HP GenomeWide siRNA of *FBXO45* was obtained from QIAGEN. The siRNA duplexes were transfected in subconfluent cells with X-treme Oligo transfection reagent following the manufacturer's instructions. The sequence of shRNA, sgRNA oligos are as follows. FBXO45 shRNA#1 5' TCTGTGTTGCCATATACAG 3', FBXO45 shRNA#2 5'

TTCCTTATCCCTTTGACAG 3', ARHGEF2 shRNA 5' CGCTCTGTCCATCGAAACTTT 3', FBXO45 sgRNA1 5' CGCTGTTCTCATCGCCGTGC 3', FBXO45 sgRNA2 5' GCACGGCGATGAGAACAGCG 3'.

RNA-sequencing

Cell populations were sorted directly into Trizol with 0.5% 2-ME and held at -80^{0}C until RNA preparation. RNA was prepared by published Trizol RNA-extraction protocol (Thermo-Fisher Scientific). RNA was co-precipitated using glycogen as a carrier. RNA was quantified using Qubit RNA high sensitivity fluorometric assay. cDNA was prepared using Takara Clonetech SMART-Seq® v4 Ultra® Low Input RNA Kit according to protocol using 500-1000 ng RNA as input. cDNA was quantified and qualified using HSDNA assay on an Agilent 2200 bioanalyzer. RNA-seq libraries were constructed using the Illumina Nextera XT kit with 150 ng cDNA input. Libraries were quality controlled and quantified by bioanalyzer and pooled at equal molar ratio prior to sequencing Illumina Hiseq (50bp SE v4 high output) and Illumina NextSeq500 (75bp SE v2 high output) machines.

Animal studies

Transgenic mice are housed in AAALAC accredited pathogen-free facility at Memorial Sloan Kettering Cancer Center. Animal studies were approved by the Institutional Animal Care & Use Committee Protocol #22-09-008).

Generation of transgenic mice with conditional deletion of Fbxo45 in germinal center B-cells

FBXO45 gene is evolutionarily conserved from *Drosophila* to mammals and the mouse *Fbxo45* gene is located on mouse chromosome 16 qB2. The gene spans 17.047 kb of genomic DNA and contains 3 exons. To investigate the functional consequences of loss of *FBXO45 in vivo*, we procured a gene trap construct from EUCOMM (http://www.eucomm.org/) which contained a conditional allele generated by insertion of 2 loxP sites into intronic sites flanking exon 2 of *FBXO45* and performed gene targeting in ES cells. Supplementary Fig. S2A illustrates the molecular design to generate conditional *Fbxo45 KO* mice (Supplementary Fig. S2A). Recombinant ES cell clones were injected into blastocysts (to generate chimeras from which germ-line transmission of the floxed allele of *FBXO45* was achieved), which were then used to generate a mouse line carrying the engineered allele. *Cre*-mediated excision of exon 2 eliminates aa residues 107 to 225 in mouse *Fbxo45* which represent the entire SPRY-domain responsible for substrate binding. Proper homologous recombination in the correct configuration resulting in deletion of exon 2 of *Fbxo45* was confirmed by multiple confirmatory PCR assays to

verify correct targeting (Supplementary Fig. S2B and S2C). A Neomycin (Neo) resistance cassette flanked by frt sites is present in the targeting vector and this was used to select targeted ES cells. The Neo cassette was deleted via flanking *frt* sites b *Flp*-recombinase by crossing the "floxed" *Fbxo45* mice with *Flp*-transgenic mice expressing Flp-recombinase. The *Fbxo45*$^{fl/-}$ mice were then bred with *Cre*-transgenic mice, expressing Cre recombinase under the control of the *Cγ1* promoter to generate the F1 generation, which allows specific deletion of *Fbxo45* in GC-derived B-cells only. F1 generation mice were intercrossed to generate age-matched cohorts of *Cγ1Cre*$^{tg/+}$-*Fbxo45*$^{fl/fl}$ (KO), *Cγ1Cre*$^{tg/+}$-*Fbxo45*$^{+/fl}$ (HET), and *Cγ1Cre*$^{tg/+}$-*Fbxo45*$^{+/+}$ (WT) littermates. Mice were born at the expected Mendelian frequencies. Deletion of *Fbxo45* in GCB-cells was confirmed by RNA Sequencing in GCB-cells isolated from spleens of mice challenged with sheep red blood cells (SRBCs) (Supplementary Fig. S2C). Conditional ablation of *Fbxo45* in transgenic mice was accomplished by *Cre*-mediated excision of exon 2 which eliminated only amino acid residues 107 to 225 in mouse Fbxo45 which represents the entire SPRY-domain responsible for substrate binding. Proper homologous recombination in the correct configuration resulted in deletion of only exon 2 while rest of the gene sequences at N terminal from aa 1-106 and C-terminal from aa 225 to 286 were unaltered and constitutes the flanking regions seen in RNA sequencing reads.

Cell stimulation

Splenocytes from 10-week-old mice were FACS-sorted into complete growth media (RPMI, 10%FBS, HEPES, Penn/Strep, NEAA, Na-Pyruvate, 2-ME). Cells were plated at 1x10^6 cells/ml in 96 well culture plates at 200μl/well. Cultures were supplemented as indicated with CpG DNA (0.1 μM), IL4 (100 ng/ml), IL5 (100 ng/ml). Cultures were incubated at 37C, 5% CO_2 for the indicated times.

Generation of transgenic Arhgef2 S644A knock-in mice

The *Arhgef2* S644A transgenic have been created by injecting Cas9 mRNA (100ng/ul), gRNA (5' tcttgagtcctttgagtccctcc3') (50-100ng/ul), and ssDNA (gctggcttcgttggaatgcccccacccgccctgcccaggggccttttttcgtcttgaggcttttgagtccctccgaggcgagcgcctgcta aaggatgccctccgtgaaggtgag) (100ng/ul) into cytoplasm of the fertilized eggs followed by transplantation of eggs into female mice. Briefly, C57BL/6J females were superovulated with injections of 5.0 IU of PMSG (BioVendor) followed by 5.0 IU of HCG (BioVendor) 48 hrs later. The females were housed with C57BL/6J males overnight and then euthanized to collect fertilized oocytes for injection. Injection mix contained gRNAs, ssDNA and Cas9 mRNA at

100ng/uL each in injection buffer (10mM Tris/0.1mM EDTA, pH 7.5). The final mix was spun twice at top speed for 30min at 4 °C to remove debris to avoid needle clogging. After cytoplasmic injection was done, C57Bl6/J zygotes were cultured overnight in the presence of SCR7 (Xcessbio) at the concentration of 50 μM. Two-cell embryos were transferred to CD-1 females by aseptic surgery and pregnancy was monitored till delivery. Pups of 10 days old were tail clipped and genotyped and analyzed for genome-editing. The use of animals in this study followed the Guide for the Care and Use of Laboratory Animals, Laboratory Animal Ordinances, and the Animal Welfare Act. This study was approved by the University of Pennsylvania Institutional Animal Care and Use Committee, protocol number 803647.

Mouse immunizations and flow cytometric analysis

For the flow analysis of GCB-cells, mice (males and females) were immunized by intraperitoneal injection of 500 million sheep red blood cells (SRBC) (Innovative Research) in 200 ul PBS, and were then analyzed after 10 days post injection., Splenic GC-cells were pre-gated on live, B220+CD19+ cells from *Cγ1Cre*$^{tg/+}$*-Fbxo45*$^{+/+}$*, Cγ1Cre*$^{tg/+}$*-Fbxo45*$^{+/fl}$*, Cγ1Cre*$^{tg/+}$*-Fbxo45*$^{fl/fl}$, and *Cγ1Cre*$^{tg/+}$*-Fbxo45*$^{fl/fl}$*; Arhgef2*$^{fl/fl}$, and *Cγ1Cre*$^{tg/+}$*-Arhgef2*$^{fl/fl}$, mice and samples were acquired on a BD LSR Fortessa cell analyzer (BD Biosciences) and were analyzed using the FlowJo software. Mann Whitney unpaired Student's T test was used for analysis (*P < 0.05, **P < 0.01, ***P < 0.001). Mice in the tumor-watch cohort (*Cγ1Cre*$^{tg/+}$*-Fbxo45*$^{+/+}$*, Cγ1Cre*$^{tg/+}$*-Fbxo45*$^{+/fl}$*, Cγ1Cre*$^{tg/+}$*-Fbxo45*$^{fl/fl}$, *Cγ1Cre*$^{tg/+}$*-Fbxo45*$^{fl/fl}$*; Arhgef2*$^{fl/fl}$, *Cγ1Cre*$^{tg/+}$*-Arhgef2*$^{fl/fl}$, *Arhgef2* S644A$^{-/-}$, *Arhgef2* S644A$^{+/-}$ and *Arhgef2* S644A$^{+/+}$) mice were subjected to chronic immunization by repeated antigenic stimulation with 5X10^{8} SRBC, delivered every two months until tumor development, death or end of the study (24 months).

Immunohistochemistry

Immunohistochemistry (IHC) staining was performed by the Laboratory of Comparative Pathology, MSKCC for CD3, CD19, and PNA using their optimized protocol. Representative IHC of PNA in germinal center (brown) and nuclei (purple) stained by hematoxylin in representative spleen sections from the same animals of the indicated genotype, 10 days post SRBC immunization. The relative germinal center area with the indicated genotype was calculated after normalization to the total spleen area. Two-tailed Mann Whitney unpaired Student's T test was used for analysis (*P < 0.05, **P < 0.01, ***P < 0.001)

Serial transplantation studies

To investigate the transplantability of lymphomas that developed in *Fbxo45*-deficient mice, we generated single cell suspensions of splenic lymphomas derived from *Fbxo45*$^{fl/fl}$-*Cγ1cre*$^{tg/+}$ (homozygous knockout) mice and performed transplantation by intravenous injection of 1X10^6 cells (secondary engraftment [n=4] and; tertiary transplant [n=6]) into immunodeficient NOD.Cg-*Prkdc*^{scid} *Il2rg*^{tm1Wjl}/SzJ (NSG) recipients. All intravenously injected mice for secondary recipients were euthanized on day 19-20 and tertiary recipients were euthanized on day 14-15 upon visual signs of discomfort identified by veterinarian staff (Supplementary Fig S4).

Plasmids

FBXO45 cDNA was cloned from a K562 cell line into pENTR/D-TOPO vector, and subcloned into a Streptavidin-Biotin-HA tandem-affinity purification (TAP)-tagged vector (kindly provided by Dr. Stephane AVngers) and TET-On inducible lentiviral vector (indigenously developed). Other HA- or FLAG-tagged F-box protein constructs were provided by Dr. Pagano. *SKP1* and *GEF-H1* cDNAs were obtained from Open Biosystems. *GEF-H1* and its mutants was cloned into pcDNA3.1-nV5, plenti6.2-cV5 (Invitrogen) and indigenously developed TET-On inducible lentiviral vector. The shRNA constructs were purchased from Sigma-Aldrich. Lentiviral vectors pGIPZ containing shRNA targeting different region of *FBXO45* (V2LHS_182000, V2LHS_222040, and V2LHS_254545) were purchased from Open Biosystems siRNA corresponding to *GEF-H1*, and Non-Specific Pool siRNA were purchased from Dharmacon (Thermo Scientific). Lentiviral packaging plasmids pMD2.G; RRID: Addgene_12259, psPAX2; RRID: Addgene_12260 and inducible Cas9 vector; RRID: Addgene_83481 was obtained from Addgene.

Protein extraction

Whole cell extracts were obtained from cell lines in the log-phase of growth or from purified mouse B-cells using lysis buffer (150 mM NaCl, 1.0%NP-40, 50mM Tris-HCl pH 8.0, 10% Glycerol, 2 mM EDTA pH 8.0) supplemented with Halt protease and phosphatase inhibitor cocktail (ThermoFisher Scientific) and 0.5 mM. phenylmethylsulfonylfluoride (PMSF), according to previously described protocols.

Immunoblot analysis

Protein extracts were resolved on 10% SDS-PAGE and transferred to PVDF membrane. Indicated antibodies were used based upon manufacturer's instructions. Quantitation of signal intensity was obtained in the ImageJ software (http://imagej.nih.gov/ij/) by subtracting the background signal (house-keeping genes) measured over signal measured for indicated protein;

areas of the same size (set on the image of the house-keeping protein) were used for all measurements. Values are expressed as fold difference relative to the house keeping protein.

Rhotekin binding domain pull-down assays for GTP-loaded RHOA

GTP-dependent RhoA binding assay was performed using the Rho Activation Assay Biochem kit (Cytoskeleton).

In vitro ubiquitylation assay

293T cells were transfected with expression vectors encoding SKP1, and FLAG-tagged FBXO45. After 48 hours of transfection, FBXO45 E3 ligase complexes were immunoprecipitated with anti-FLAG resin. GEF-H1 WT and GEF-H1 S644A mutant were cloned in pET28a vector engineered to tag 10X histidine followed by a sumo-tag at the N-terminus as a fusion protein. HIS-tagged GEF-H1 proteins were solubilized in His- purification buffer (50mM HEPES-NaOH pH 8.0, 150mM Nacl, 10mM Imidazole), sonicated at 5 amplitude for 5 cycles of 1 minute sonication/1 minute at ice. Lysates were centrifuged at 20,000xg for 90 min and clear supernatant was aspirated into new tubes, and the soluble GEF H1 protein was purified from the supernatant using standard His-tag purification procedure using NiNTA matrix, washed, and incubated in the presence of 2mM MgATP, 1.5ng/µL E1 (R&D system), 10 ng/µL UBE2D3 (R&D system), 10 ng/mL UBE2R1 (R&D system), 1 µM human ubiquitin protein (R&D system), and protease inhibitor cocktail (Calbiochem) for 16 hour at 30°C. The reaction mixture was centrifuged and the supernatant was aspirated into fresh tubes, sample prepared in LSB and analyzed by western blotting. His-tagged GEF-H1 proteins immobilized on Ni-NTA matrix were washed with 8 bed volume of His-tag purification buffer. HIS–tagged GEF- H1 (WT and S644A mutant) were eluted using 200 mM Imidazole in HIS-purification buffer and analyzed by western blotting.

Sanger sequencing

B-cell lymphoma cell lines iBJAB (i=doxycycline inducible Cas9) lacking *FBXO45* were generated using inducible CRISPR-Cas9 strategy to knockout *FBXO45* (*iBJAB KO*). *FBXO45* gene was amplified from Isogenic clones and separated by 1% Agarose Gel and photographed, the bands were gel excised and submitted for sequencing analysis and validated for deletion using sanger sequencing.

Pseudoalignment and gene expression

Transcript abundance was computed by pseudoalignment with Kallisto (62,63). Transcript per million (TPM) values were then normalized and fitted to a linear model by empirical Bayes

method with the Voom and Limma R packages (64) and differential gene expression was defined as a Benjamini and Hochberg corrected p-value of <0.05 and fold change > 2 unless otherwise noted.

Generation of CRISPR-Cas9-mediated FBXO45 knockout (KO) cells

FBXO45 was targeted for CRISPR/inducible CAS9 mediated knockout to evaluate the function of gene. In this regard, three oligos were designed at N-terminal region of *FBXO45* to incorporate frameshift-mediated premature termination of FBXO45 translation. Briefly, first K562(FLAG-*FBXO45*) and BJAB, cells were stably transduced with *Cas9* gene under the control of doxycycline induction using lentiviral delivery. Cells were selected with blasticidin-s-hydrochloride (10μg/ml) for 10 days. Cells were further transduced with plasmids containing sgRNA targeting N-terminal region of *FBXO45*. The plasmid harboring sgRNA also carry GFP as reporter for evaluation of stable transduction. The targeting sgRNA were cloned and sequence verified.

After stable transduction, four isogenic clones showing expression of GFP as surrogate for sgRNA expression were isolated and expanded using manufacturer's protocol. (ClonaCell™ TCS medium, Stem Cell Technologies, Cat No# 03814). Isolated clones were induced with doxycycline 2 μg/ml for 72 hours and again isolated using manufacturer's protocol. (ClonaCell™ TCS medium, Stem Cell Technologies, Cat No# 03814). Knockout of *FBXO45* was analyzed by Sanger sequencing analysis of amplified *FBXO45* gene from isogenic clones (Supplementary Fig S5A and S5G).

Xenograft studies

A total of 1.0 $X10^6$ iBJAB (i = Inducible Cas9 with *FBXO45-WT* or *FBXO45 KO*) tumor cell clones were inoculated in NSG mice. At D10 (day 10), the mice were treated with 1mg/kg Trametinib by oral gavage daily for 2 weeks. tumor growth was monitored by relative size. *In vivo* imaging studies show decreased tumor sizes in response to Trametinib treatment in FBXO45 KO xenografts. At the end of the study, tumors were circumscribed for imaging, and tumor growth was assessed by determining tumor volume measurements. Percent tumor growth inhibition (%TGI) at indicated days after Trametinib treatments in *FBXO45*-depleted xenografts and measured compared to controls. Tumor volumes of mice treated with Trametinib (n = 6 each) for both iBJAB-KO vs iBJAB-WT were individually measured every three days and plotted graphically. Experiments were performed in triplicate.

Establishment of a bioluminescent model of transformed DLBCL

FL518$^{GFP\text{-}Luciferase,\ NS\ shRNA}$ and FL518$^{GFP\text{-}Luciferase,\ FBXO45\ shRNA}$ cells at density of 0.5x 10^6/100µl of PBS in matrigel suspension in the ratio of 1:1 were injected subcutaneously in both flanks of 4~6-week-old NSG mice (n=8). Bioluminescence imaging (BLI) of the tumor growth was performed from day of injection to 5 days, the time point when the tumor was visible. At this point, we administered corn oil (vehicle) or Trametinib (1mg/kg body weight via oral gavage) every day until the termination of the experiment.Prior to BLI mice received an intraperitoneal injection with D-Luciferin. Fifteen minutes after D-Luciferin injection, animals were anesthetized for 5 minutes and subjected to *in vivo* imaging.

Whole genome sequencing analysis

The whole genome sequencing data for patient samples was obtained from the previously published study by Dreval et al. (40). For the analyses outlined here, we have excluded the analysis cohorts COM and post-HT as defined in the Dreval et al. study, and have grouped the no-HT with pre-HT patients into single group FL. The somatic mutations, copy number variations (CNV), and structural variants (SV) were detected as previously described in details (40,65). The SV affecting the *FBXO45* and *ARHGEF2* loci were defined as intrachromosomal events with breakpoints within 1 Mbp region from the gene of interest and were manually reviewed in the Integrated Genome Viewer (IGV) for artifacts. For the downstream analysis, small duplications and deletions at target genes were combined together with copy number alterations for the tumors where no CNV was identified. When necessary, the multiple test correction was conducted using the Benjamini and Hochberg method for all statistical analyses. *P*-values below 0.05 and *Q*-values below 0.1 where multiple test correction was necessary were considered significant.

Fluorescence in situ hybridization

Fluorescence *in situ* hybridization (FISH) was performed using standard protocols on formalin-fixed paraffin-embedded (FFPE) tissues or cryoslides obtained from patients with diagnosis of FL and DLBCL, FISH probes were created based on samples that were subjected to whole genome sequencing (International Cancer Genome Consortium; Germinal Center B-cell Lymphoma; ICGC MMML-Seq) (Supplementary Table S5 and S6). Based on genomic breakpoints delineated by WGS of the germinal center B-cell lymphomas targeting *FBXO45* (3q29) and *ARHGEF2* (1q22), we generated and labelled FISH probes to identify copy number variations (CNV) affecting the corresponding genomic loci. Genomic coordinates and assignments were based on UCSC Genome Build 18.

For CNVs encompassing *FBXO45*, we generated probes (Red label) from BAC clones (Empire Genomics); RP11-481O2 spanning genomic region 197,700,426-197,871,782 and RP11-74H7 spanning nucleotides 197,710,756 to 197,896,969 respectively, on chromosome 3. The chromosome 3 Control Probe at 3p11.1. was generated using BAC clone (SKU CHR03-10-GR) Green Label. The probes to detect genomic loci encompassing *ARHGEF2* were RP11-867L17 spanning nucleotides 154,063,168 to 154,247,821, and RP11-838A18 spans nucleotides 154,153,803 to 154,338,433 on chromosome 1. The BAC clone SKU CHR01-10-GR) was used to generate the control probe at 1q11.1-1q11.2 (Green label). The appropriate probes were applied and hybridization and washing performed according to standard procedures (60). A total of 100 nuclei were examined for each probe whenever possible. Digital image acquisition, processing and evaluation were performed using ISIS digital image analysis version 5.0 (MetaSystems, Altussheim, Germany).

Cell viability and proliferation assays

Cell viability was estimated by trypan blue exclusion method followed by cell counting and cell proliferation evaluation was performed by counting of cells using TC20 automated cell counter (Bio-Rad).

Biopsies and fixed paraffin-embedded tissues (FFPE)

Samples were studied in accordance with the ethics and principles of the Declaration of Helsinki. Specimens were all fixed FFPE obtained as part of the diagnostic protocol for routine management. The studies were approved by the University of Pennsylvania Institutional Review Board IRB (Protocol #826234).

Mycoplasma testing and authentication of cell lines

Mycoplasma testing of all the cell lines used in the study were routinely performed using Universal Mycoplama Detection Kit (ATCC # 30-1012K) following manufacturer's instructions. Authentication of all cell lines used in this study were performed by ATCC cell line authentication service with STR profile report.

Statistical analysis

Statistical analysis were performed using GraphPad Prism 5 (GraphPad Software). Student's t test or one-way ANOVA were performed using the assumptions of the test. For sample sizes $n = 3$, a two-tailed unpaired Student's T-test was utilized when variance between two groups was similar. For sample sizes greater than $n = 3$, normally distributed data were analyzed using a two-tailed unpaired Student's T-test when variances were similar. Data that were not distributed

normally were analyzed using a Mann-Whitney test. Z-score was used to calculate standard deviation from mean in shRNA colony formation screen. Error bars shown in the Figures represent the mean ± s.d. or s.e.m. Kaplan-Meier curves and survival analysis were performed using a long-rank test to evaluate statistical differences between the tested groups. The *P* values are described in the Figure legends. Statistically significant differences are represented in the manuscript text, Figures and legends as: **P*<0.05, ***P*<0.01, ****P*<0.001, *****P*<0.0001.

Data and Resource Availability

All data generated or analyzed during this study are included in this article and its supplementary information files. Specifically, source data and statistics for non–high-throughput experiments such as flow cytometry, qPCR, protein experiments, and other molecular or cellular assays are provided in Supplementary Table S7. Original cell lines and genetically modified cell lines are available via the Elenitoba-Johnson lab. The data that was generated at BC was deposited at https://ega-archive.org/studies/EGAS00001006646. ICGC data as bam files from DACO project are deposited at https://ega-archive.org/studies/EGAS00001002199. The NCI data as bam files through dfGAP project are deposited at https://www.ncbi.nlm.nih.gov/projects/gap/cgi-bin/study.cgi?study_id=phs000235.v20.p6. Information about Cancer Genome Characterization Initiative projects can be found at https://ocg.cancer.gov/programs/cgci. Most data, reagents, methods, and materials that support the findings of this research are available from the corresponding author upon reasonable request. Some material used in the reported research may require requests to collaborators and agreements with other entities. Requests are reviewed by MSKCC to verify whether the request is subject to any intellectual property or confidentiality obligations. Any material that can be shared will be released via a Material Transfer Agreement.

REFERENCES

1. Klein U, Dalla-Favera R. Germinal centres: role in B-cell physiology and malignancy. Nat Rev Immunol **2008**;8(1):22-33 doi 10.1038/nri2217.
2. Teras LR, DeSantis CE, Cerhan JR, Morton LM, Jemal A, Flowers CR. 2016 US lymphoid malignancy statistics by World Health Organization subtypes. CA Cancer J Clin **2016**;66(6):443-59 doi 10.3322/caac.21357.

3. Swerdlow SH, Campo E, Pileri SA, Harris NL, Stein H, Siebert R*, et al.* The 2016 revision of the World Health Organization classification of lymphoid neoplasms. Blood **2016**;127(20):2375-90 doi 10.1182/blood-2016-01-643569.
4. Montoto S, Davies AJ, Matthews J, Calaminici M, Norton AJ, Amess J*, et al.* Risk and clinical implications of transformation of follicular lymphoma to diffuse large B-cell lymphoma. J Clin Oncol **2007**;25(17):2426-33 doi 10.1200/JCO.2006.09.3260.
5. Link BK, Maurer MJ, Nowakowski GS, Ansell SM, Macon WR, Syrbu SI*, et al.* Rates and outcomes of follicular lymphoma transformation in the immunochemotherapy era: a report from the University of Iowa/MayoClinic Specialized Program of Research Excellence Molecular Epidemiology Resource. J Clin Onco **2013** l;31(26):3272-8.
6. Kuppers R, Klein U, Hansmann ML, Rajewsky K. Cellular origin of human B-cell lymphomas. N Engl J Med **1999**;341(20):1520-9 doi 10.1056/NEJM199911113412007.
7. Pasqualucci L. The germinal center in the pathogenesis of B cell lymphomas. Hematol Oncol **2023**;41 Suppl 1:62-9 doi 10.1002/hon.3141.
8. Nalepa G, Rolfe M, Harper JW. Drug discovery in the ubiquitin-proteasome system. Nat Rev Drug Discov **2006**;5(7):596-613 doi 10.1038/nrd2056.
9. Frescas D, Pagano M. Deregulated proteolysis by the F-box proteins SKP2 and beta-TrCP: tipping the scales of cancer. Nat Rev Cancer **2008**;8(6):438-49 doi nrc2396 [pii] 10.1038/nrc2396.
10. Babbitt SE, Kiss A, Deffenbaugh AE, Chang YH, Bailly E, Erdjument-Bromage H*, et al.* ATP hydrolysis-dependent disassembly of the 26S proteasome is part of the catalytic cycle. Cell **2005**;121(4):553-65.
11. Bai C, Sen P, Hofmann K, Ma L, Goebl M, Harper JW*, et al.* SKP1 connects cell cycle regulators to the ubiquitin proteolysis machinery through a novel motif, the F-box. Cell **1996**;86(2):263-74 doi S0092-8674(00)80098-7 [pii].
12. Cenciarelli C, Chiaur DS, Guardavaccaro D, Parks W, Vidal M, Pagano M. Identification of a family of human F-box proteins. Curr Biol **1999**;9(20):1177-9 doi 10.1016/S0960-9822(00)80020-2.
13. Jin J, Cardozo T, Lovering RC, Elledge SJ, Pagano M, Harper JW. Systematic analysis and nomenclature of mammalian F-box proteins. Genes Dev **2004**;18(21):2573-80 doi 18/21/2573 [pii] 10.1101/gad.1255304.

14. Skowyra D, Craig KL, Tyers M, Elledge SJ, Harper JW. F-box proteins are receptors that recruit phosphorylated substrates to the SCF ubiquitin-ligase complex. Cell **1997**;91(2):209-19.
15. Vashisht AA, Zumbrennen KB, Huang X, Powers DN, Durazo A, Sun D*, et al.* Control of iron homeostasis by an iron-regulated ubiquitin ligase. Science **2009**;326(5953):718-21 doi 1176333 [pii]
10.1126/science.1176333.
16. Wertz IE, Kusam S, Lam C, Okamoto T, Sandoval W, Anderson DJ*, et al.* Sensitivity to antitubulin chemotherapeutics is regulated by MCL1 and FBW7. Nature **2011**;471(7336):110-4.
17. Skaar JR, Pagan JK, Pagano M. SCF ubiquitin ligase-targeted therapies. Nat Rev Drug Discov **2014**;13(12):889-903 doi 10.1038/nrd4432.
18. Saiga T, Fukuda T, Matsumoto M, Tada H, Okano HJ, Okano H*, et al.* Fbxo45 forms a novel ubiquitin ligase complex and is required for neuronal development. Mol Cell Biol **2009**;29(13):3529-43 doi MCB.00364-09 [pii]
10.1128/MCB.00364-09.
19. Liao EH, Hung W, Abrams B, Zhen M. An SCF-like ubiquitin ligase complex that controls presynaptic differentiation. Nature **2004**;430(6997):345-50 doi 10.1038/nature02647 nature02647 [pii].
20. Jaffe AB, Hall A. Rho GTPases: biochemistry and biology. Annu Rev Cell Dev Biol **2005**;21:247-69 doi 10.1146/annurev.cellbio.21.020604.150721.
21. Rossman KL, Der CJ, Sondek J. GEF means go: turning on RHO GTPases with guanine nucleotide-exchange factors. Nat Rev Mol Cell Biol **2005**;6(2):167-80 doi nrm1587 [pii] 10.1038/nrm1587.
22. Glaven JA, Whitehead IP, Nomanbhoy T, Kay R, Cerione RA. Lfc and Lsc oncoproteins represent two new guanine nucleotide exchange factors for the Rho GTP-binding protein. J Biol Chem **1996**;271(44):27374-81.
23. Ren Y, Li R, Zheng Y, Busch H. Cloning and characterization of GEF-H1, a microtubule-associated guanine nucleotide exchange factor for Rac and Rho GTPases. J Biol Chem **1998**;273(52):34954-60 doi 10.1074/jbc.273.52.34954.

24. Joo E, Olson MF. Regulation and functions of the RhoA regulatory guanine nucleotide exchange factor GEF-H1. Small GTPases **2021**;12(5-6):358-71 doi 10.1080/21541248.2020.1840889.
25. Whitehead I, Kirk H, Tognon C, Trigo-Gonzalez G, Kay R. Expression cloning of lfc, a novel oncogene with structural similarities to guanine nucleotide exchange factors and to the regulatory region of protein kinase C. J Biol Chem **1995**;270(31):18388-95.
26. Eva A, Vecchio G, Rao CD, Tronick SR, Aaronson SA. The predicted DBL oncogene product defines a distinct class of transforming proteins. Proc Natl Acad Sci U S A **1988**;85(7):2061-5.
27. Hart MJ, Eva A, Evans T, Aaronson SA, Cerione RA. Catalysis of guanine nucleotide exchange on the CDC42Hs protein by the dbl oncogene product. Nature **1991**;354(6351):311-4 doi 10.1038/354311a0.
28. Krendel M, Zenke FT, Bokoch GM. Nucleotide exchange factor GEF-H1 mediates cross-talk between microtubules and the actin cytoskeleton. Nat Cell Biol **2002**;4(4):294-301 doi 10.1038/ncb773
ncb773 [pii].
29. Cerione RA, Zheng Y. The Dbl family of oncogenes. Curr Opin Cell Biol **1996**;8(2):216-22.
30. Quilliam LA, Khosravi-Far R, Huff SY, Der CJ. Guanine nucleotide exchange factors: activators of the Ras superfamily of proteins. Bioessays **1995**;17(5):395-404 doi 10.1002/bies.950170507.
31. Ron D, Tronick SR, Aaronson SA, Eva A. Molecular cloning and characterization of the human dbl proto-oncogene: evidence that its overexpression is sufficient to transform NIH/3T3 cells. EMBO J **1988**;7(8):2465-73.
32. Marcotte R, Brown KR, Suarez F, Sayad A, Karamboulas K, Krzyzanowski PM*, et al.* Essential gene profiles in breast, pancreatic, and ovarian cancer cells. Cancer Discov **2012**;2(2):172-89.
33. Mizuarai S, Yamanaka K, Kotani H. Mutant p53 induces the GEF-H1 oncogene, a guanine nucleotide exchange factor-H1 for RhoA, resulting in accelerated cell proliferation in tumor cells. Cancer Res **2006**;66(12):6319-26 doi 10.1158/0008-5472.CAN-05-4629.

34. Cullis J, Meiri D, Sandi MJ, Radulovich N, Kent OA, Medrano M*, et al.* The RhoGEF GEF-H1 is required for oncogenic RAS signaling via KSR-1. Cancer Cell **2014**;25(2):181-95 doi 10.1016/j.ccr.2014.01.025.
35. Cheng IK, Tsang BC, Lai KP, Ching AK, Chan AW, To KF*, et al.* GEF-H1 over-expression in hepatocellular carcinoma promotes cell motility via activation of RhoA signalling. J Pathol **2012**;228(4):575-85.
36. Liao YC, Ruan JW, Lua I, Li MH, Chen WL, Wang JR*, et al.* Overexpressed hPTTG1 promotes breast cancer cell invasion and metastasis by regulating GEF-H1/RhoA signalling. Oncogene **2012**;31(25):3086-97 doi 10.1038/onc.2011.476.
37. Ravid T, Hochstrasser M. Diversity of degradation signals in the ubiquitin-proteasome system. Nat Rev Mol Cell Biol **2008**;9(9):679-90 doi nrm2468 [pii] 10.1038/nrm2468.
38. Morey TM, Esmaeili MA, Duennwald ML, Rylett RJ. SPAAC Pulse-Chase: A Novel Click Chemistry-Based Method to Determine the Half-Life of Cellular Proteins. Front Cell Dev Biol **2021**;9:722560 doi 10.3389/fcell.2021.722560.
39. Imami K, Yasuda T. Measuring Protein Synthesis during Cell Cycle by Azidohomoalanine (AHA) Labeling and Flow Cytometric Analysis. Bio Protoc **2019**;9(8):e3215 doi 10.21769/BioProtoc.3215.
40. Dreval K, Hilton LK, Cruz M, Shaalan H, Ben-Neriah S, Boyle M*, et al.* Genetic subdivisions of follicular lymphoma defined by distinct coding and noncoding mutation patterns. Blood **2023**;142(6):561-73 doi 10.1182/blood.2022018719.
41. Wright GW, Huang DW, Phelan JD, Coulibaly ZA, Roulland S, Young RM*, et al.* A Probabilistic Classification Tool for Genetic Subtypes of Diffuse Large B Cell Lymphoma with Therapeutic Implications. Cancer Cell **2020**;37(4):551-68 e14 doi 10.1016/j.ccell.2020.03.015.
42. Skaar JR, Pagan JK, Pagano M. Mechanisms and function of substrate recruitment by F-box proteins. Nat Rev Mol Cell Biol **2013**;14(6):369-81 doi 10.1038/nrm3582.
43. Nakayama KI, Nakayama K. Ubiquitin ligases: cell-cycle control and cancer. Nat Rev Cancer **2006**;6(5):369-81 doi 10.1038/nrc1881.
44. Randle SJ, Laman H. F-box protein interactions with the hallmark pathways in cancer. Semin Cancer Biol **2016**;36:3-17.

45. Zheng N, Shabek N. Ubiquitin Ligases: Structure, Function, and Regulation. Annu Rev Biochem **2017**;86:129-57.
46. Bassermann F, Eichner R, Pagano M. The ubiquitin proteasome system - implications for cell cycle control and the targeted treatment of cancer. Biochim Biophys Acta **2014**;1843(1):150-62 doi 10.1016/j.bbamcr.2013.02.028.
47. Wang Z, Liu P, Inuzuka H, Wei W. Roles of F-box proteins in cancer. Nat Rev Cancer **2014**;14(4):233-47 doi 10.1038/nrc3700.
48. Duan S, Pagano M. Ubiquitin ligases in cancer: Functions and clinical potentials. Cell Chem Biol **2021**;28(7):918-33 doi 10.1016/j.chembiol.2021.04.008.
49. Duan S, Cermak L, Pagan JK, Rossi M, Martinengo C, di Celle PF*, et al.* FBXO11 targets BCL6 for degradation and is inactivated in diffuse large B-cell lymphomas. Nature **2012**;481(7379):90-3 doi 10.1038/nature10688.
50. Pighi C, Cheong TC, Compagno M, Patrucco E, Arigoni M, Olivero M*, et al.* Frequent mutations of FBXO11 highlight BCL6 as a therapeutic target in Burkitt lymphoma. Blood Adv **2021**;5(23):5239-57 doi 10.1182/bloodadvances.2021005682.
51. Schneider C, Kon N, Amadori L, Shen Q, Schwartz FH, Tischler B*, et al.* FBXO11 inactivation leads to abnormal germinal-center formation and lymphoproliferative disease. Blood **2016**;128(5):660-6 doi 10.1182/blood-2015-11-684357.
52. Peschiaroli A, Scialpi F, Bernassola F, Pagano M, Melino G. The F-box protein FBXO45 promotes the proteasome-dependent degradation of p73. Oncogene **2009**;28(35):3157-66 doi 10.1038/onc.2009.177.
53. Chen X, Sahasrabuddhe AA, Szankasi P, Chung F, Basrur V, Rangnekar VM*, et al.* Fbxo45-mediated degradation of the tumor-suppressor Par-4 regulates cancer cell survival. Cell Death Differ **2014**;21(10):1535-45 doi 10.1038/cdd.2014.92.
54. Wu L, Yu K, Chen K, Zhu X, Yang Z, Wang Q*, et al.* Fbxo45 facilitates pancreatic carcinoma progression by targeting USP49 for ubiquitination and degradation. Cell Death Dis **2022**;13(3):231 doi 10.1038/s41419-022-04675-2.
55. Lin XT, Yu HQ, Fang L, Tan Y, Liu ZY, Wu D*, et al.* Elevated FBXO45 promotes liver tumorigenesis through enhancing IGF2BP1 ubiquitination and subsequent PLK1 upregulation. Elife **2021**;10 doi 10.7554/eLife.70715.

56. Gygi SP, Rist B, Griffin TJ, Eng J, Aebersold R. Proteome analysis of low-abundance proteins using multidimensional chromatography and isotope-coded affinity tags. J Proteome Res **2002**;1(1):47-54 doi 10.1021/pr015509n.
57. Wolters DA, Washburn MP, Yates JR, 3rd. An automated multidimensional protein identification technology for shotgun proteomics. Anal Chem **2001**;73(23):5683-90 doi 10.1021/ac010617e.
58. Han DK, Eng J, Zhou H, Aebersold R. Quantitative profiling of differentiation-induced microsomal proteins using isotope-coded affinity tags and mass spectrometry. Nat Biotechnol **2001**;19(10):946-51 doi 10.1038/nbt1001-946.
59. von Haller PD, Yi E, Donohoe S, Vaughn K, Keller A, Nesvizhskii AI*, et al.* The application of new software tools to quantitative protein profiling via isotope-coded affinity tag (ICAT) and tandem mass spectrometry: II. Evaluation of tandem mass spectrometry methodologies for large-scale protein analysis, and the application of statistical tools for data analysis and interpretation. Mol Cell Proteomics **2003**;2(7):428-42 doi 10.1074/mcp.M300041-MCP200.
60. Ventura RA, Martin-Subero JI, Jones M, McParland J, Gesk S, Mason DY*, et al.* FISH analysis for the detection of lymphoma-associated chromosomal abnormalities in routine paraffin-embedded tissue. J Mol Diagn **2006**;8(2):141-51 doi 10.2353/jmoldx.2006.050083.
61. Rolland DCM, Basrur V, Jeon YK, McNeil-Schwalm C, Fermin D, Conlon KP*, et al.* Functional proteogenomics reveals biomarkers and therapeutic targets in lymphomas. Proc Natl Acad Sci U S A **2017**;114(25):6581-6 doi 10.1073/pnas.1701263114.
62. Law CW, Chen Y, Shi W, Smyth GK. voom: Precision weights unlock linear model analysis tools for RNA-seq read counts. Genome Biol **2014**;15(2):R29 doi 10.1186/gb-2014-15-2-r29.
63. Ritchie ME, Phipson B, Wu D, Hu Y, Law CW, Shi W*, et al.* limma powers differential expression analyses for RNA-sequencing and microarray studies. Nucleic Acids Res **2015**;43(7):e47 doi 10.1093/nar/gkv007.
64. Casola S, Cattoretti G, Uyttersprot N, Koralov SB, Seagal J, Hao Z*, et al.* Tracking germinal center B cells expressing germ-line immunoglobulin gamma1 transcripts by conditional gene targeting. Proc Natl Acad Sci U S A **2006**;103(19):7396-401 doi 10.1073/pnas.0602353103.

65. Thomas N, Dreval K, Gerhard DS, Hilton LK, Abramson JS, Ambinder RF, *et al.* Genetic subgroups inform on pathobiology in adult and pediatric Burkitt lymphoma. Blood **2023**;141(8):904-16 doi 10.1182/blood.2022016534.

FIGURE LEGENDS

Figure 1. *In vivo* conditional targeting of *Fbxo45* in GCB-cells of transgenic mice results in abnormal GCB-cell expansion. Representative flow plots **A,** and quantification **B,** of germinal center (GC) cells pre-gated on live, B220+CD19+ splenic cells from *Cγ1Cre*$^{tg/+}$*-Fbxo45*$^{+/+}$, *Cγ1Cre*$^{tg/+}$*-Fbxo45*$^{+/fl}$, *Cγ1Cre*$^{tg/+}$*-Fbxo45*$^{fl/fl}$ mice analyzed 10 days post-SRBC stimulation. **A,** Numbers in each panel indicate the frequencies of germinal center, B220+ B-cells identified by CD95+PNA+. **B,** Graphs show percentages of GCB-cells/spleen identified by CD95+PNA+ (n = number of mice per genotype at 4-6 months of age). **C,** Graph shows the percentages of GCB-cells/spleen identified by CD95+GL7+ (n = number of mice per genotype at 4-6 months of age). Two-tailed Mann Whitney unpaired Student's T test was used for analysis (*P < 0.05, **P < 0.01, ***P < 0.001). **D,** Graph shows the absolute number of GCB-cells/spleen of SRBC immunized mice from the indicated genotype. Two-tailed Mann Whitney unpaired Student's T test was used for analysis (*P < 0.05, **P < 0.01, ***P < 0.001). **E,** Graph shows the number of GC/spleen of SRBC immunized mice from the indicated genotype. Data is representative of three independent experiments. Two-tailed Mann Whitney unpaired Student's T test was used for analysis (*P < 0.05, **P < 0.01, ***P < 0.001). **F,** Graph shows the area of GC (pixel^2)/spleen after normalization to the total spleen area of SRBC immunized mice from the indicated genotype. Two-tailed Mann Whitney unpaired Student's T test was used for analysis (*P < 0.05, **P < 0.01, ***P < 0.001). **G,** IHC images of PNA in GC (brown) and nuclei (purple) stained by hematoxylin in representative spleen sections from indicated genotype, 10 days post SRBC immunization. **H,** Quantitative analysis of PNA stained sections of spleen was performed using Image J software. The quantification is represented as mean ± SEM of pixel intensity.

Figure 2. *In vivo* conditional deletion and haploinsufficiency of *Fbxo45* in GCB-cells results in B-cell lymphomagenesis. **A,** Kaplan-Meier survival curves color coded for the indicated genotype. **B,** Homozygous *Fbxo45* knockout mice (*Cγ1Cre*$^{tg/+}$*-Fbxo45*$^{fl/fl}$) develop lymphomas. Representative images from 3 different animals with lymphoma masses circumscribed in green.

Top left panel: Large cervical lymphoma. Middle and lower left panel: Visceral lymphoma masses and retroperitoneal lymph nodes extensively involved by lymphoma. Right panel shows weight of mesenteric lymph nodes compared between *Cγ1Cre$^{tg/+}$-Fbxo45$^{+/+}$* and *Cγ1Cre$^{tg/+}$-Fbxo45$^{fl/fl}$* mice. **C,** Left panel: representative images of large ileocecal lymphomas from 3 *Cγ1Cre$^{tg/+}$-Fbxo45$^{fl/fl}$* animals juxtaposed to Peyer's patches (white circles) from 5 *Cγ1Cre$^{tg/+}$-Fbxo45$^{+/+}$* animals. Right panel shows volume of lymph nodes from *Cγ1Cre$^{tg/+}$-Fbxo45$^{fl/fl}$* compared to *Cγ1Cre$^{tg/+}$-Fbxo45$^{+/+}$* mice. **D,** Left panel: representative images of spleen from 3 pairs of *Cγ1Cre$^{tg/+}$-Fbxo45$^{+/+}$* and *Cγ1Cre$^{tg/+}$-Fbxo45$^{fl/fl}$* littermates. Box and whisker plots show significantly (****P<0.0001) increased spleen size in *Cγ1Cre$^{tg/+}$-Fbxo45$^{fl/fl}$* compared to *Cγ1Cre$^{tg/+}$-Fbxo45$^{+/+}$* mice. **E,** Immunohistochemical (IHC) staining of FL and DLBCL in *Cγ1Cre$^{tg/+}$-Fbxo45$^{fl/fl}$* mice as indicated. **F,** Percent incidences of lymphomagenesis among *Cγ1Cre$^{tg/+}$-Fbxo45$^{+/+}$, Cγ1Cre$^{tg/+}$-Fbxo45$^{+/fl}$, and Cγ1Cre$^{tg/+}$-Fbxo45$^{fl/fl}$* transgenic mice. **G,** Next generation sequencing analysis of *IGHV* gene usage to assess clonal populations in tumors from *Cγ1Cre$^{tg/+}$-Fbxo45$^{fl/fl}$* mice.

Figure 3. FBXO45 regulates GEF-H1 protein stability, RhoA activation and colony formation. **A,** Venn diagram showing overlap of proteins from quantitative proteomic analysis of *Cγ1Cre$^{tg/+}$-Fbxo45$^{fl/fl}$* GCB-cells compared with GCB-cells from *Cγ1Cre$^{tg/+}$-Fbxo45$^{+/+}$* transgenic mice, and proteins enriched in FBXO45 immunoprecipitation and identified by MS/MS. **B,** BJAB cells expressing TET-inducible FLAG-tagged FBXO45 (iFLAG FBXO45) were induced with vehicle control or doxycycline (2ug/ml) for 72 hours followed by immunoprecipitation (IP) using FLAG-resin. The whole cell extract (WCE) and IP were immunoblotted with the indicated antibodies. **C,** HEK293 cells expressing empty vector (EV) or the indicated FLAG-tagged (FBXW1, FBXL1, FBXW2, FBXW4, FBXW5, FBXW7, FBXO45, FBXO22) F-box proteins were subjected to immunoprecipitation (IP) as indicated and analyzed along with whole cell extract (WCE) by western blotting (WB) as indicated **D,** Splenic germinal center B-cells were isolated and pooled GCB-cells from *Cγ1Cre$^{tg/+}$-Fbxo45$^{+/+}$* and pooled GCG-cells from *Cγ1Cre$^{tg/+}$-Fbxo45$^{fl/fl}$* transgenic mice are subjected to cycloheximide pulse chase experiments to measure GEF-H1 protein turnover. WCLs were immunoblotted with the indicated antibodies. **E,** *FBXO45* mRNA levels were analyzed by qRT-PCR in BJAB cells stably transduced with two different target shRNA oligos for *FBXO45*. The housekeeping gene *GAPDH* was used as control. **F,** BJAB$^{NS\ shRNA}$ (non-

specific) and BJAB$^{FBXO45\ shRNA}$ #1, and #2 *shRNA* expressing cells treated with cycloheximide (CHX) for given time points were evaluated by WB as indicated. **G,** BJAB$^{NS\ shRNA}$ and BJAB$^{FBXO45\ shRNA}$ #1, and #2 *shRNA* expressing cells were tested using methyl-cellulose colony formation assays. Viable colonies after 3 weeks were counted and the data (±s.d.) from three independent experiments are presented. **H,** BJAB$^{NS\ shRNA}$ and BJAB$^{FBXO45\#2\ shRNA}$ cells treated with cycloheximide (CHX) for given time points were evaluated by WB. The WCE was immunoprecipitated using active RhoA purification kit and analyzed for active RhoA. The same WCE was analyzed by WB for GEF-H1, RhoA and GAPDH. **I,** The doxycycline-inducible FLAG-FBXO45 expressing BJAB cells were treated with vehicle or Doxycycline (4µg/ml) as indicated and the WCE was immunoprecipitated using active RhoA purification kit and analyzed for active RhoA. The same WCE was analyzed by WB for GEF-H1, RhoA and GAPDH. "Created with BioRender.com"

Figure 4. Abnormal expansion of GCB-compartment and subsequent lymphomagenesis observed in Fbxo45-deficient mice are reverted by co-deletion of *Arhgef2*. **A,** Schematic illustration of the strategy used to generate the indicated genotype. Representative flow plots **B,** and quantification **C,** of GCB-cells pre-gated on live, B220+CD19+ splenic cells from *Cγ1Cre*$^{tg/+}$-*Fbxo45*$^{+/+}$ (n=10), *Cγ1Cre*$^{tg/+}$-*Fbxo45*$^{fl/fl}$ (n=9), *Cγ1Cre*$^{tg/+}$-*Fbxo45*$^{fl/fl}$; -*Arhgef2*$^{fl/fl}$ (n=5) and *Cγ1Cre*$^{tg/+}$-*Arhgef2*$^{fl/fl}$ (n=3) 4-6 months old mice analyzed 10 days post SRBC stimulation as indicated. Numbers in each panel indicate the frequencies of GC, B220+ B-cells depicted by CD95+PNA+ staining. Graphs showing the percentages of GCB-cells. Data are representative of three independent experiments. Mann Whitney unpaired Student's T test was used for analysis (*P < 0.05, **P < 0.01). **D,** Percent incidences of lymphomagenesis among *Cγ1Cre*$^{tg/+}$-*Fbxo45*$^{+/+}$ (n=20), *Cγ1Cre*$^{tg/+}$-*Fbxo45*$^{fl/fl}$ (n=20), *Cγ1Cre*$^{tg/+}$-*Fbxo45*$^{fl/fl}$; *Arhgef2*$^{fl/fl}$ (n=11) transgenic mice (****P<0.0001). **E,** Immunohistochemical (IHC) staining of *Cγ1Cre*$^{tg/+}$-*Fbxo45*$^{+/+}$, *Cγ1Cre*$^{tg/+}$-*Fbxo45*$^{fl/fl}$, and *Cγ1Cre*$^{tg/+}$-*Fbxo45*$^{fl/fl}$; *Arhgef2*$^{fl/fl}$ mice as indicated (scale bar =1 mm). Inset shows PNA at higher magnification (scale bar= 50 µm). "Created with BioRender.com"

Figure 5. GEF-H1 S644 is critical for interaction with FBXO45 and GEF-H1 polyubiquitylation. **A,** 293T cells were transfected with HA-tagged FBXO45 or empty vector (EV). At 48 hours after transfection, WCE were treated with λ protein phosphatase (λ-PPase) with or without phosphatase inhibitor (PI) for 30 min and subjected to IP with anti-HA resin followed by blotting with the indicated antibodies. **B,** Schematic illustration of deletion map of GEF-H1. **C,** HEK293

cells co-expressing HA-tagged FBXO45 and the indicated V5-tagged truncated GEF-H1 mutants were immunoprecipitated (IP) as indicated and analyzed by western blotting (WB) for the indicated proteins. **D,** Alignment of the amino acids corresponding to the binding region in human GEF-H1 and other species. A conserved serine 644 residue among GEF-H1 from various species examined (highlighted in red). The numbers indicate the position of the amino acid residue. **E,** HEK293 cells co-expressing HA-tagged FBXO45 and V5-tagged GEF-H1 WT or GEF-H1 S644A mutant were treated with MG132 (10μM) for 6 hours, immunoprecipitated with anti-V5 or anti-HA resin, and analyzed by WB for the indicated proteins. **F,** BJAB cells stably expressing doxycycline-inducible "i" FLAG-tagged GEF-H1 WT and GEF-H1 S644A mutant were transiently transduced with lentiviral particles containing HA-tagged FBXO45. Cells were induced with doxycycline for 72 hours (4 μg/ml) followed by MG132 treatment (10 μM) for 6 hours. WCE were subjected to IP and analyzed by WB as indicated. **G,** *E. coli* purified 10XHistidine tagged-GEF-H1 WT or GEF-H1 S644A mutant was stained by Coomassie brilliant blue to validate its purity and was subjected to *in vitro* ubiquitylation assay using purified UBE2R1, UBE2D3, UBE1, ubiquitin, Mg-ATP, PLK1 and immunopurified FBXO45 E3 ligase complex from HEK293 cells. The reaction was immunoblotted for indicated antibodies.

Figure 6. *In vivo* transgenic knock-in of *Arhgef2* S644A results in disseminated B-cell lymphoma. **A,** Schematic illustration of design of constitutional *Arhgef2* S644A knock-in transgenic mice where *Arhgef2 S644 WT* express wild-type gene, *Arhgef2 S644A* +/- is heterozygous knock-in and *Arhgef2 S644A* +/+ is homozygous knock-in. **B,** Sanger sequencing chromatogram from *Arhgef2 S644 WT* (WT) and *Arhgef2 S644A* +/+ (homozygous) knock-in. Serine 644(S644) encoded by codon "TCC" is mutated to Alanine(A) encoded by codon "GCT" resulting in the S644A mutant Arhgef2 protein. **C,** Splenic B-cells from *Arhgef2 S644 WT* and *Arhgef2 S644A* +/+ mice were analyzed after cycloheximide pulse chase experiment for GEF-H1 protein turnover. GAPDH serves as loading control. **D,** Band intensity was measured using image J from three independent experiments and plotted to show GEF-H1 protein turnover. Error bars represent ±s.d. (n = 3) ***P < 0.001. **E,** Percent incidences of lymphomagenesis among *Arhgef2 S644 WT Arhgef2 S644A +/-,* and *Arhgef2 S644A* +/+ knock-in transgenic mice. **F,** Left panel, gross image of the abdominal organs between *Arhgef2 S644 WT*, and *Arhgef2 S644A* +/+ mice showing enlarged liver in homozygous mice, right panel shows representative image of liver and spleen compared between *Arhgef2 S644 WT* and *Arhgef2 S644A* +/+ mice

as indicated. **G,** IHC staining as indicated. (**H**) Next generation sequencing analysis of *IGHV* gene usage to assess clonal populations in *Arhgef2 S644A* +/+ mice.

Figure 7. *FBXO45* deficiency sensitizes B-cell lymphoma to MAPK pathway inhibition *in vitro* and *in vivo*. **A,** *FBXO45* wild-type (*WT*) or CRISPR-Cas9-mediated *FBXO45* knockout (*KO*) iBJAB ("I"= doxycycline inducible Cas9 expression) cells were treated with cycloheximide (CHX) and WCE was analyzed by WB with indicated antibodies. **B,** *FBXO45 WT* and *KO* iBJAB cells were treated with Trametinib as indicated and WCEs were analyzed by WB with the indicated antibodies **C,** *FBXO45 WT* and *KO* iBJAB cells were xenografted in NSG mice and treated with Trametinib as detailed in the Methods section. Tumor volumes of mice treated with Trametinib for both *FBXO45 WT* and *KO* (n = 6 each) were individually measured every three days and plotted graphically. Experiments were performed in triplicate. **D,** *In vivo* imaging studies at day 25 show decreased tumor sizes in response to Trametinib treatment in *FBXO45* KO xenografts. At the end of the study (Day 25), tumors were surgically removed for imaging analysis as shown in right panel. **E,** the upper panel shows a schematic illustration of the experimental plan to evaluate Trametinib treatment on xenograft tumors originated by FL518-CBG luciferase cells. The lower panel shows representative bioluminescence imaging at the day 1, day 6, day 8 and day 13. **F,** Relative bioluminescence for each group of mice was measured and plotted for day 13. Two-tailed Mann Whitney unpaired Student's T test was used for analysis (*P < 0.05, **P < 0.01, ***P < 0.001). **G,** Kaplan-Meier survival curves of *NS* shRNA and *FBXO45* shRNA expressing FL518-derived lymphoma xenografts in SCID-BEIGE mice. Log-rank (Mantel-Cox) Test was used for analysis.

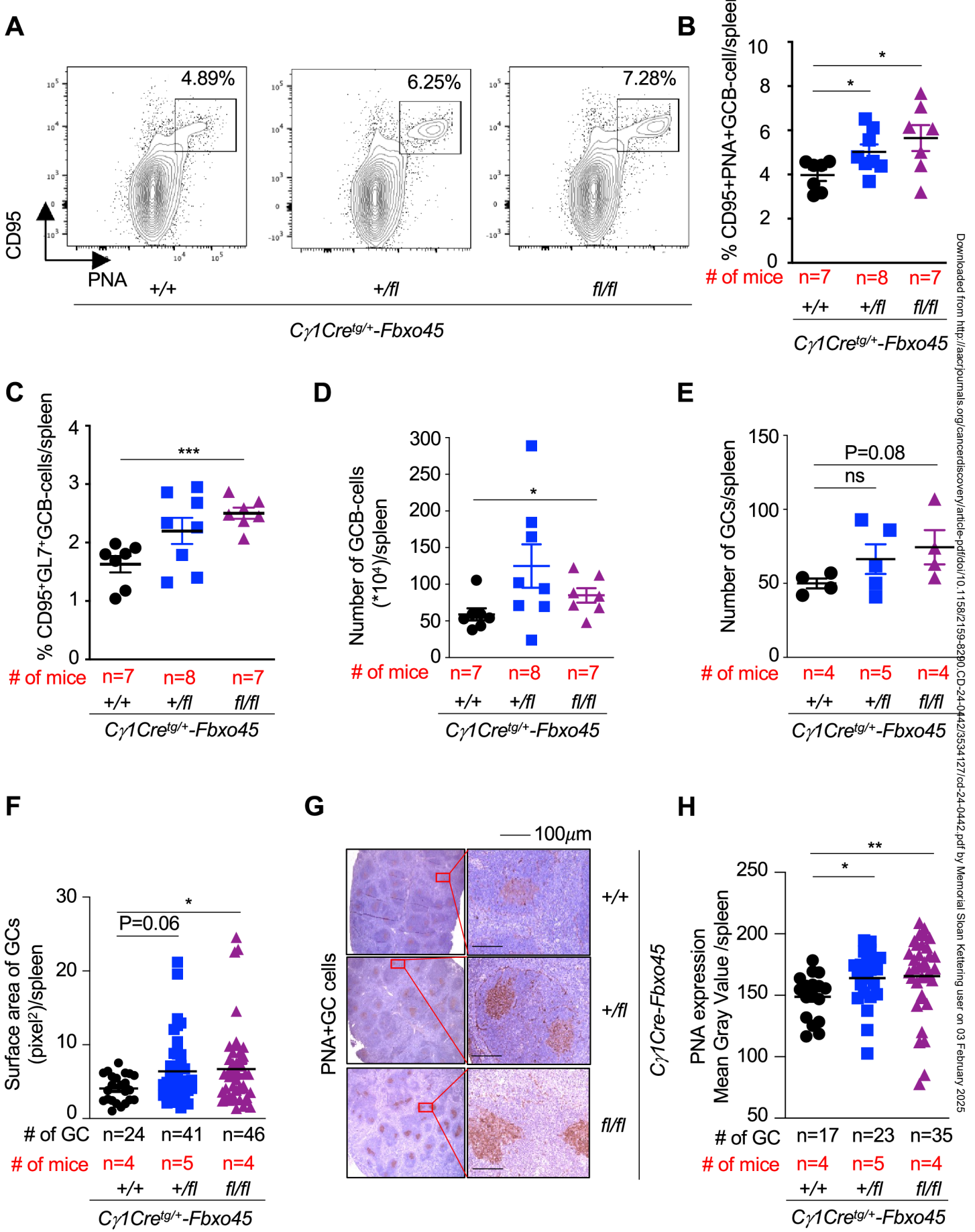

Figure 1. *In vivo* conditional targeting of *Fbxo45* in GCB-cells of transgenic mice results in abnormal GCB-cell expansion

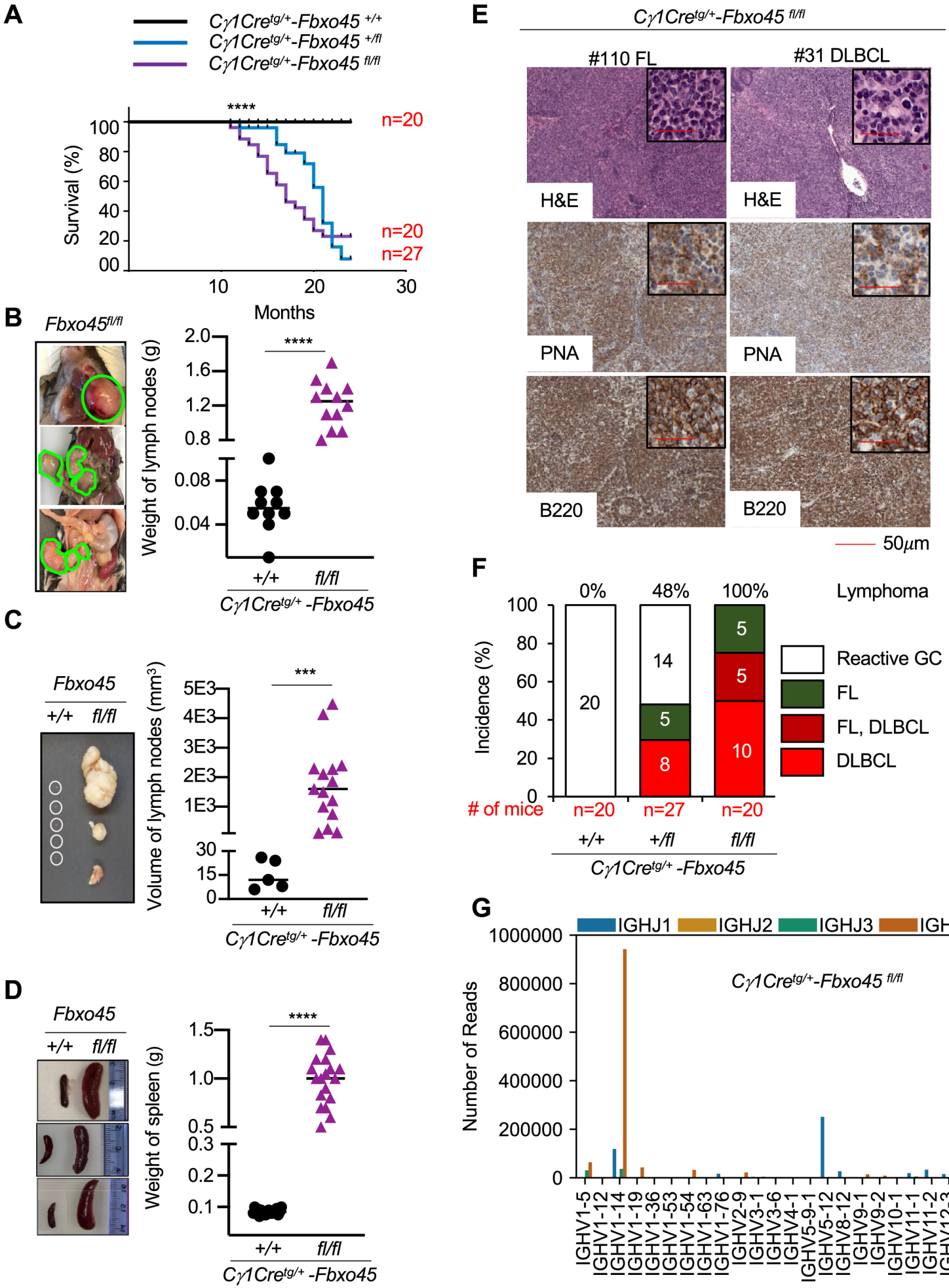

Figure 2. *In vivo* conditional deletion and haploinsufficiency of *Fbxo45* in GCB-cells results in B-cell lymphomagenesis

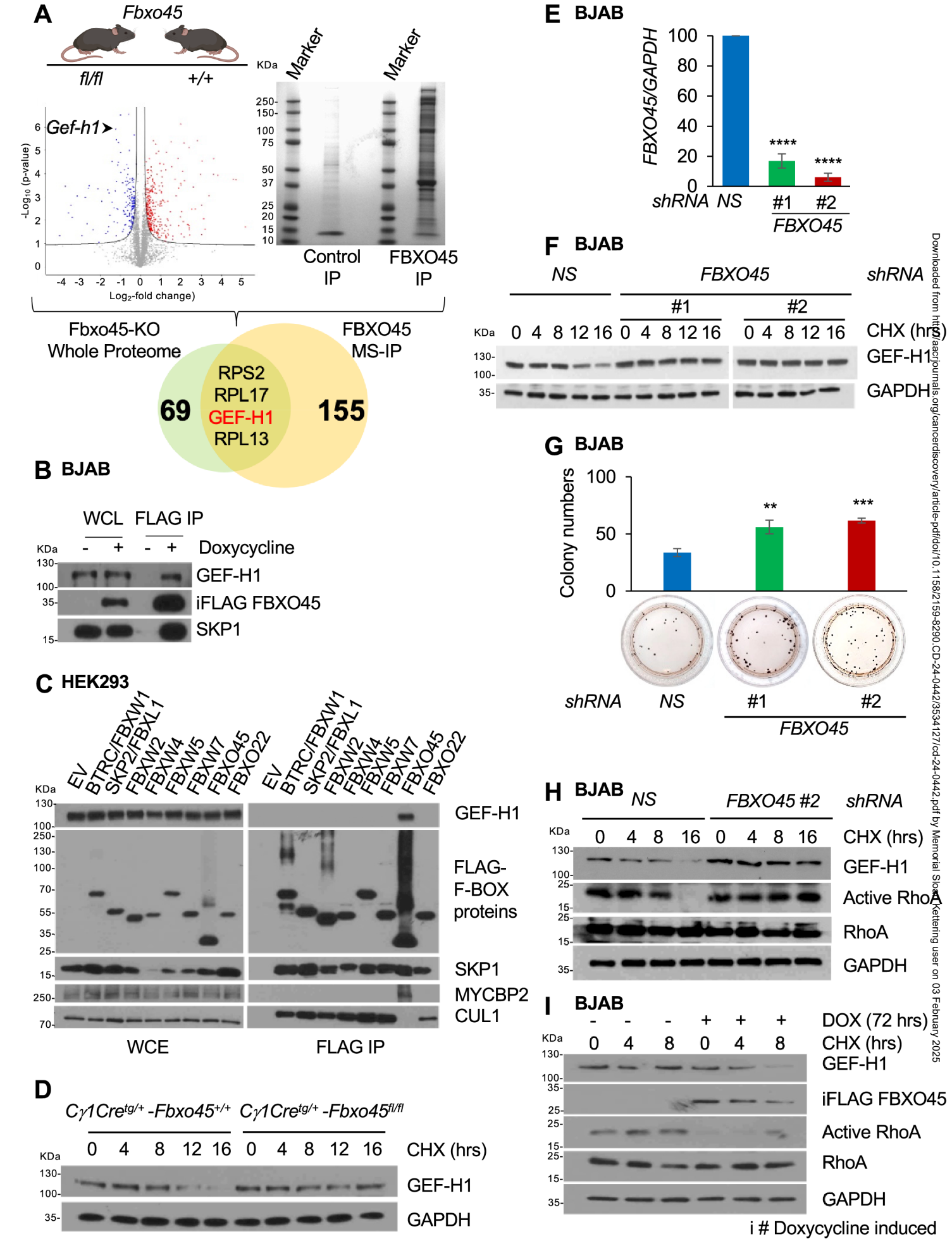

Figure 3. FBXO45 regulates GEF-H1 protein stability, RhoA activation and colony formation

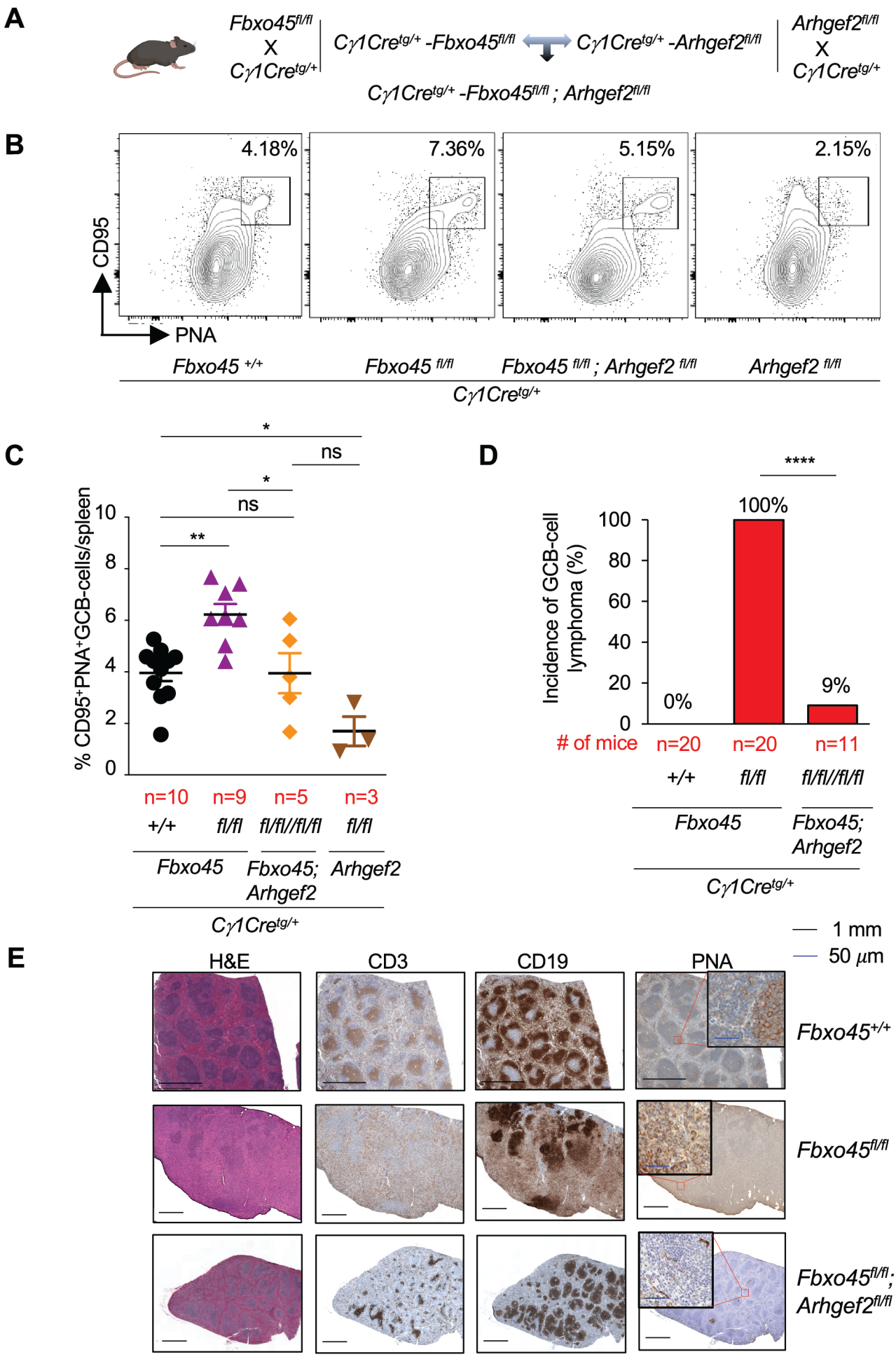

Figure 4. Abnormal expansion of the GCB-compartment and subsequent lymphomagenesis observed in *Fbxo45*-deficient mice are reverted by co-deletion of *Arhgef2*.

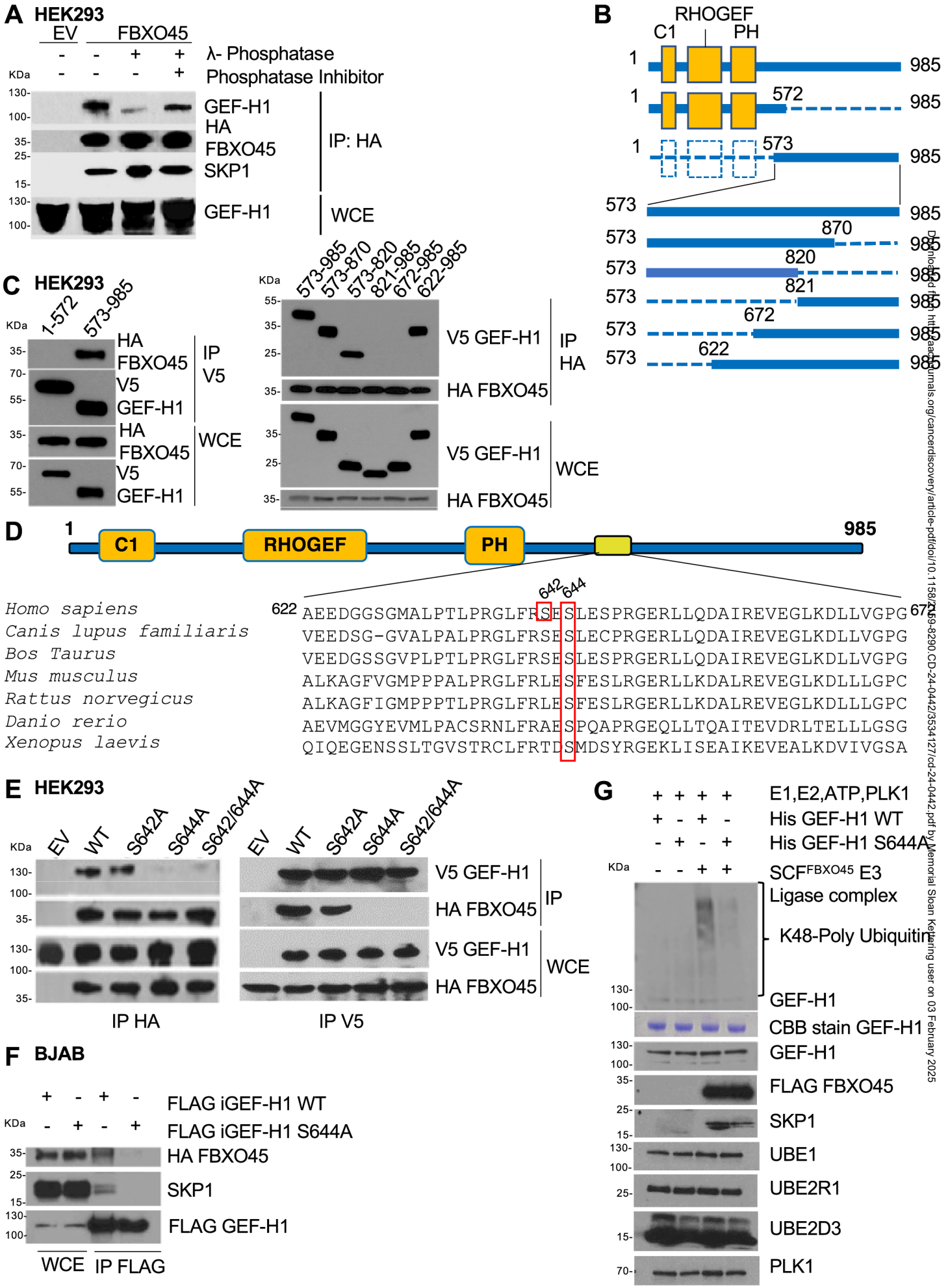

Figure 5. GEF-H1 S644 is critical for interaction with FBXO45 and GEF-H1 polyubiquitylation

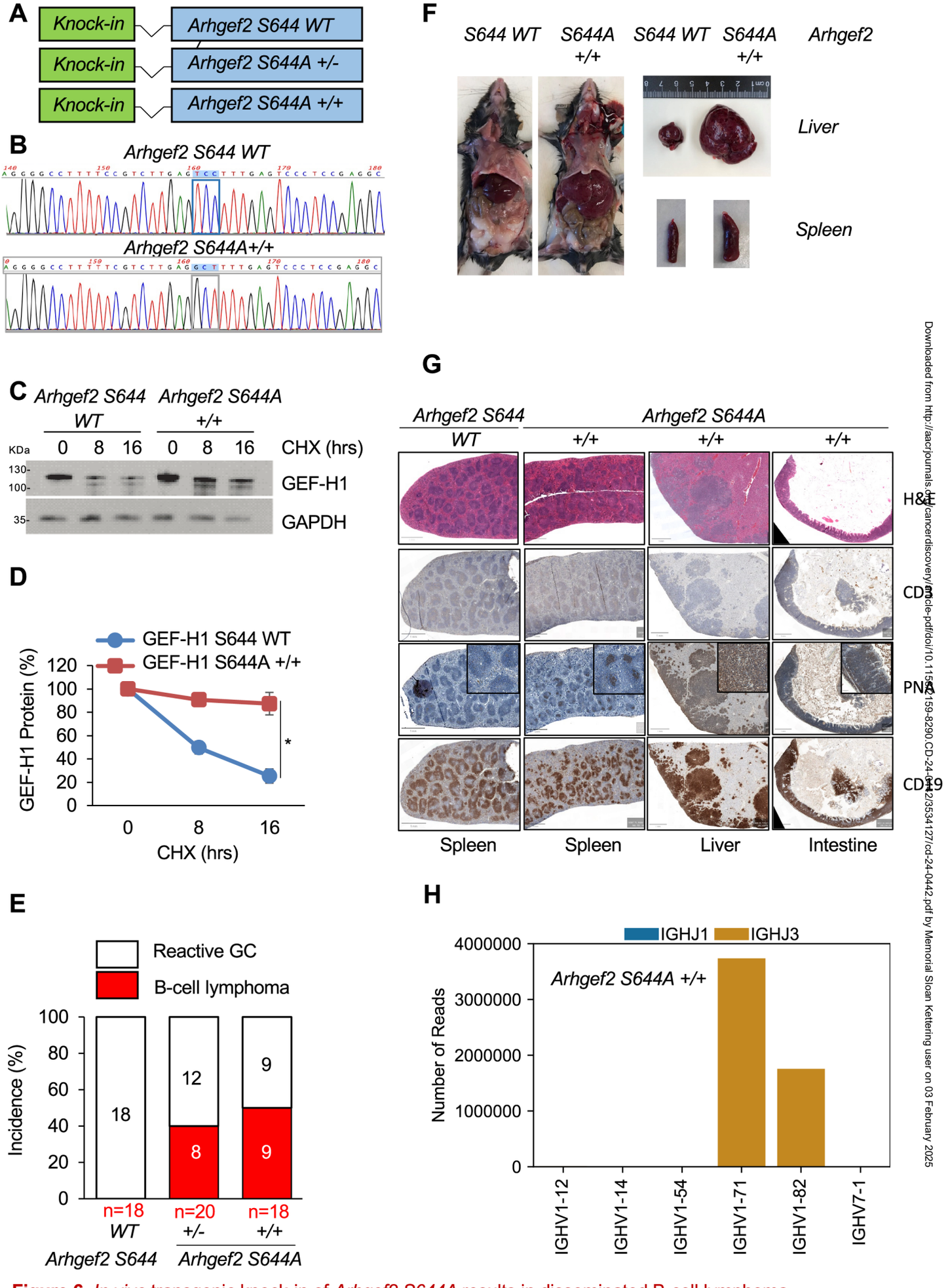

Figure 6. *In vivo* transgenic knock-in of *Arhgef2 S644A* results in disseminated B-cell lymphoma.

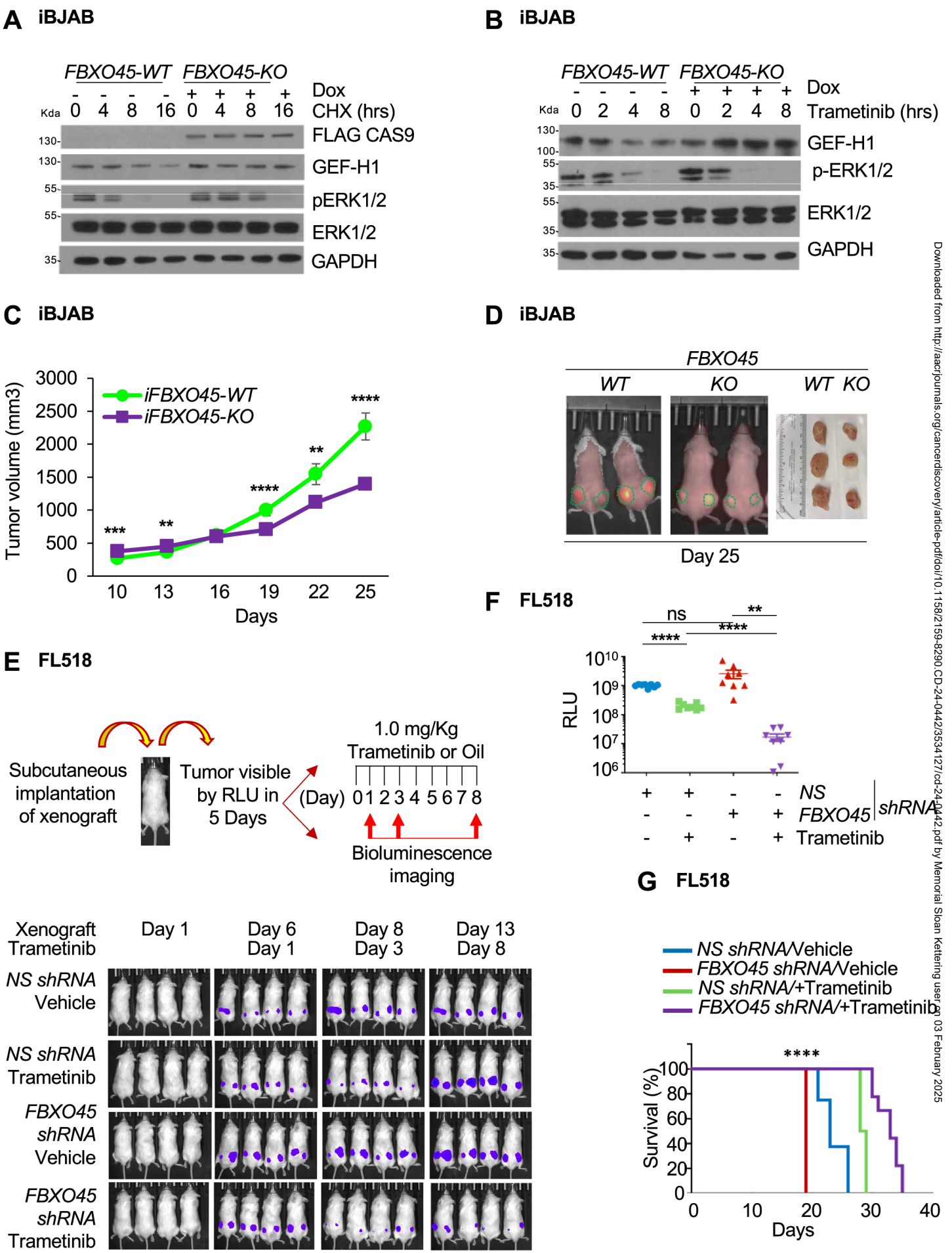

Figure 7. *FBXO45* deficiency sensitizes B-cell lymphoma to MAPK pathway inhibition *in vitro* and *in vivo*